Neuron

Article

Specific populations of basal ganglia output neurons target distinct brain stem areas while collateralizing throughout the diencephalon

Graphical abstract

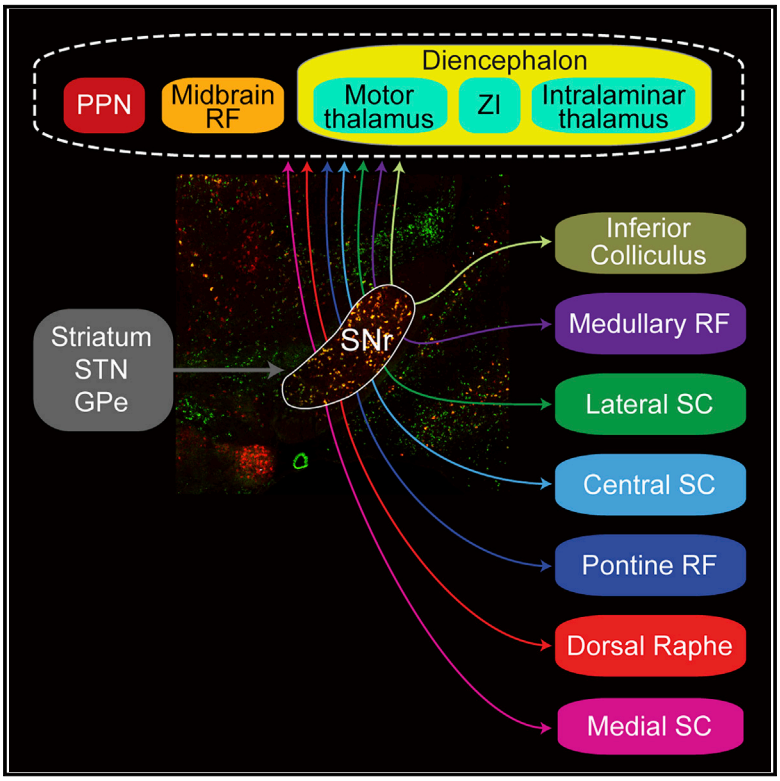

Highlights

- SNr neurons project to diverse structures throughout the diencephalon and brain stem
- Neuronal subsets project differentially and strongly to distinct brain stem targets
- Neuronal subsets differ in their subthreshold and spiking electrophysiology
- Neuronal subsets additionally form collaterals that universally target PPN and thalamus

Authors

Lauren E. McElvain, Yuncong Chen, Jeffrey D. Moore, ..., Byung Kook Lim, Rui M. Costa, David Kleinfeld

Correspondence

rc3031@columbia.edu (R.M.C.), dk@physics.ucsd.edu (D.K.)

In brief

McElvain et al. map the complete set of brain-wide projections from the largest output nucleus of the murine basal ganglia, the *substantia nigra pars reticulata*. Spatially segregated and electrophysiologically distinct subpopulations are revealed that project to different brain stem regions along with extensive collaterals to the pedunculopontine nucleus and diencephalon targets.

McElvain et al., 2021, Neuron *109*, 1721–1738
May 19, 2021 © 2021 Elsevier Inc.
https://doi.org/10.1016/j.neuron.2021.03.017

CellPress

Neuron

CellPress

Article

Specific populations of basal ganglia output neurons target distinct brain stem areas while collateralizing throughout the diencephalon

Lauren E. McElvain,[1,2,3] Yuncong Chen,[4,7] Jeffrey D. Moore,[5,7] G. Stefano Brigidi,[2] Brenda L. Bloodgood,[2] Byung Kook Lim,[2] Rui M. Costa,[3,6,*] and David Kleinfeld[1,2,8,*]

[1]Department of Physics, University of California, San Diego, La Jolla, CA 92093, USA
[2]Section of Neurobiology, University of California, San Diego, La Jolla, CA 92093, USA
[3]Champalimaud Neuroscience Programme, Champalimaud Centre for the Unknown, Lisbon 1400-038, Portugal
[4]Department of Computer Science, University of California, San Diego, La Jolla, CA 92093, USA
[5]Department of Molecular and Cellular Biology, Harvard University, Cambridge, MA 02138, USA
[6]Zuckerman Institute and Department of Neuroscience, Columbia University, New York, NY 10027, USA
[7]These authors contributed equally
[8]Lead contact
*Correspondence: rc3031@columbia.edu (R.M.C.), dk@physics.ucsd.edu (D.K.)
https://doi.org/10.1016/j.neuron.2021.03.017

SUMMARY

Basal ganglia play a central role in regulating behavior, but the organization of their outputs to other brain areas is incompletely understood. We investigate the largest output nucleus, the *substantia nigra pars reticulata* (SNr), and delineate the organization and physiology of its projection populations in mice. Using genetically targeted viral tracing and whole-brain anatomical analysis, we identify over 40 SNr targets that encompass a roughly 50-fold range of axonal densities. Retrograde tracing from the volumetrically largest targets indicates that the SNr contains segregated subpopulations that differentially project to functionally distinct brain stem regions. These subpopulations are electrophysiologically specialized and topographically organized and collateralize to common diencephalon targets, including the motor and intralaminar thalamus as well as the pedunculopontine nucleus and the midbrain reticular formation. These findings establish that SNr signaling is organized as dense, parallel outputs to specific brain stem targets concurrent with extensive collateral branches that encompass the majority of SNr axonal boutons.

INTRODUCTION

Motor actions are the consequence of neuronal computations in circuits that are distributed broadly across the nervous system (Grillner, 2006; Kuypers, 2011; Towe and Luschei, 2013). Individual components of the motor system have been studied extensively, with prominent attention given to the cerebral cortex, basal ganglia, and cerebellum. These studies have yielded deep insights into local signaling within each structure (Klaus et al., 2019; Peters et al., 2017; Raymond and Medina, 2018). However, the organization and circuit mechanisms that connect nodes of the motor system to each other remain largely unknown.

Here we investigate the circuit basis by which outputs of the basal ganglia impinge on the broader motor system. Basal ganglia form an essential component of the volitional motor system and mediate fundamental aspects of behavioral regulation and learning (Alexander et al., 1990; Hikosaka et al., 2014; Jin and Costa, 2015; Turner and Desmurget, 2010). Disruption of the basal ganglia network underlies common movement disorders, including Parkinson's disease and Tourette syndrome (Mink, 2001; Nelson and Kreitzer, 2014), and impairs control of the limbs, trunk, and facial, oral, and vocal musculature (DeLong and Georgopoulos, 2011; Robbins et al., 1986; Visser and Bloem, 2005). Moreover, basal ganglia dysfunction has also been implicated in cognitive and affective control.

Neurons in the volumetrically largest output nucleus of the basal ganglia, the *substantia nigra pars reticulata* (SNr), emit well-established projections to the superior colliculus, motor and intralaminar thalamic nuclei, and the pedunculopontine nucleus (PPN) (Alexander et al., 1990; Hikosaka, 2007b; Mena-Segovia et al., 2004). However, the extent to which projections to well-established targets arise from the same or segregated neurons is debated (Anderson and Yoshida, 1977; Beckstead and Frankfurter, 1982; Deniau et al., 1977; Parent et al., 1983). SNr neurons exhibit heterogeneous firing responses during behavior (DeLong et al., 1983; Gulley et al., 2002; Hikosaka and Wurtz, 1983; Jin and Costa, 2010), suggesting that the nucleus might contain functionally distinct projection types. Moreover, evidence from past studies indicates that the SNr projects to additional domains of the brain stem and diencephalon (Cebrián et al., 2005; Chronister et al., 1988; Gervasoni et al., 2000; Pollak Dorocic et al., 2014; Schneider et al., 1985; Takakusaki et al., 2003; Von Krosigk and Smith, 1991; Yasui et al., 1992). The lack of systematic circuit mapping has hindered comprehensive

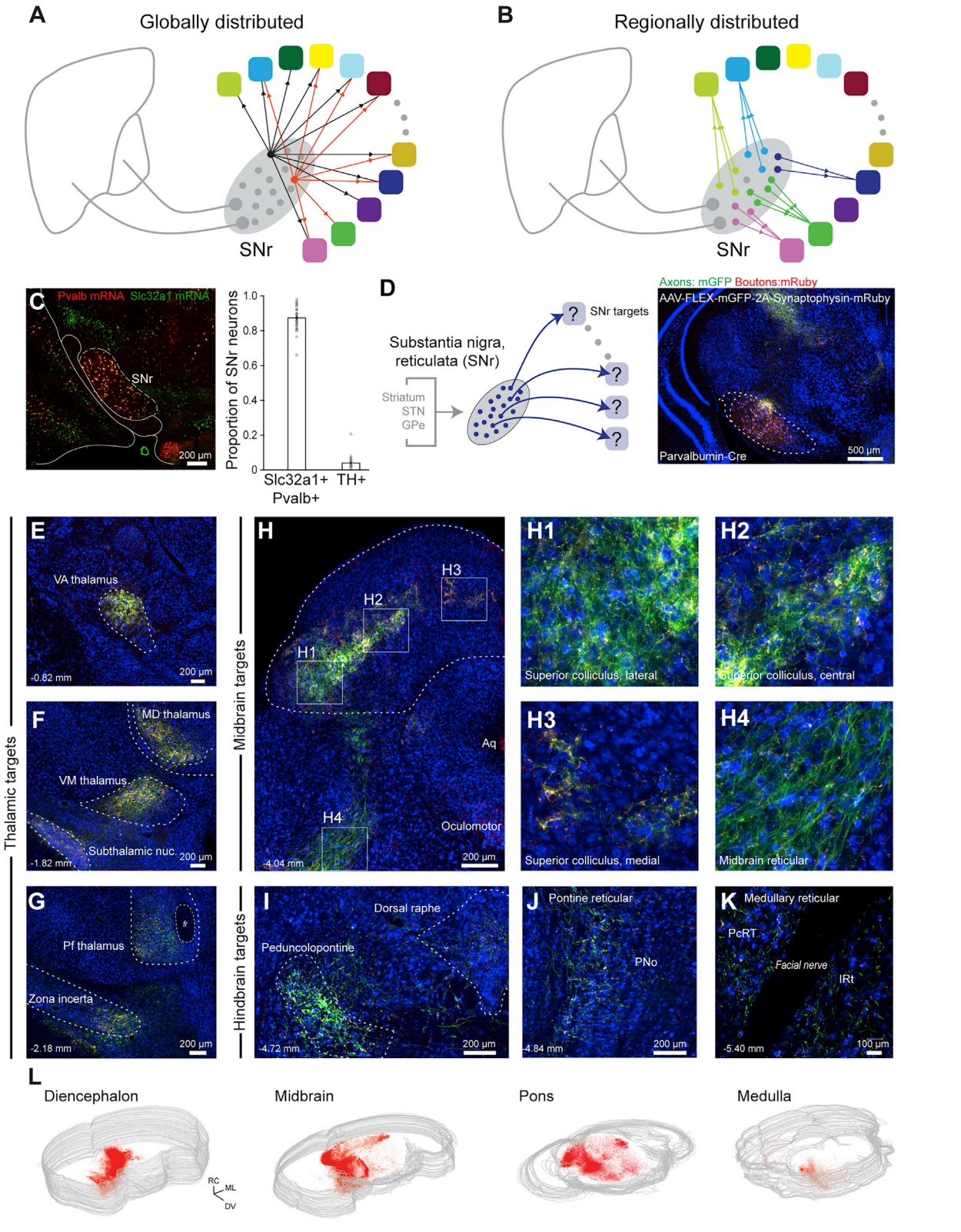

(legend on next page)

identification of SNr target regions, and it remains unknown whether the SNr contains distinct classes of projection neurons.

To delineate the circuit logic of basal ganglia output signaling and projection cell types in the SNr, we first address the mesoscopic organization of SNr projections and determine the electrophysiological properties of SNr neurons. (1) Which brain regions are the major targets of SNr axonal projections? (2) Do different electrophysiological properties of SNr cells correspond to distinct output populations? (3) Do neurons in the SNr project equally to all major targets, as expected for a global hub-like architecture (Figure 1A), or does the SNr contain segregated projection populations that project preferentially to different targets (Figure 1B)? To address these questions, we combine state-of-the-art viral circuit mapping; high-resolution, whole-brain optical scanning; and electrophysiological recordings of identified projection neurons.

RESULTS

The SNr projects broadly to diverse brain stem and thalamic regions

To identify the brain regions targeted by basal ganglia outputs, we mapped SNr axonal projections and synaptic terminals across the brain using genetically restricted viral tracing. The predominant population of neurons in the SNr is parvalbumin-positive GABAergic neurons (González-Hernández and Rodríguez, 2000). We verified that 86.9% ± 1.0% of GABAergic SNr neurons express parvalbumin (14,901 neurons, 39 sections, 4 mice) (Figures 1C and S1A–S1C) throughout the rostral-caudal extent of the nucleus (Figure S1B). To label the axons and presynaptic boutons arising from this population, membrane-bound green fluorescent protein (mGFP) and synaptophysin-mRuby were expressed virally (AAV-DJ-hSyn-FLEX-mGFP-2A-synaptophysin-mRuby) in SNr neurons in parvalbumin-Cre (PV-Cre) mice (Figure 1D). High-resolution, whole-brain slide scanning of SNr projections reveals axon terminations that extend over 7 mm, from the anterior thalamus to the caudal brain stem (Figures 1E–1L).

In the diencephalon, SNr targets include major motor (ventromedial [VM] and ventroanterior [VA]) and intralaminar/midline (mediodorsal [MD], centro-lateral/medial [CL/CM], and parafascicular [Pf]) thalamic nuclei (Figures 1E–1G), as in other species (Cebrián et al., 2005; Graybiel and Ragsdale, 1979; Utter and Basso, 2008), as well as the thalamic reticular nucleus, *zona incerta* (ZI), fields of Forel, and prerubral field (Figures S2A–S2G). A greater number of targets are observed in the brain stem. Beyond well-established projections to the superior colliculus and PPN (Hikosaka, 2007b; Figures 1H and 1I), extensive SNr projections target volumetrically large domains of the midbrain reticular formation (MidRF), pontine reticular formation (PNo), and medullary reticular formation (Med; subdivisions parvicellular [PcRT] and intermediate [IRT]) as well as 17 small premotor nuclei (Figures 1H–1K, S2H–S2K, and S3). Downstream brain stem targets span regions that have been implicated in oculomotor and head orientation (superior colliculus, INC/MA3/Su3; Fukushima, 1987; May et al., 2019), orofacial sensorimotor systems (Med, Su5, P5, and L5; Kolta et al., 2010; McElvain et al., 2018), hindlimb control (PNo; Brownstone and Chopek, 2018), and neuromodulation (PPN and dorsal raphe [DR]) and nuclei implicated in heterogeneous or unknown functions; i.e., the precuneiform nucleus, red nucleus, subdivisions of the periaqueductal gray (PAG), and parabrachial nuclei (Figures S2 and S3). We identified significant SNr projections to 42 distinct regions (Figure 2A).

GABAergic neurons throughout the extent of SNr express parvalbumin, encoded by the gene Pvalb (Figures 1C and S1), and GAD2 mRNA (Figure S1C), with large neurons in the dorsolateral SNr highly expressing parvalbumin and smaller neurons in the VM SNr expressing lower levels (Figure S1A; González-Hernández et al., 2001; González-Hernández and Rodríguez, 2000). To test whether the smaller percentage of parvalbumin-negative SNr GABAergic neurons project to distinct downstream targets, we performed additional axonal tracing from the SNr in VGAT-Cre mice (Figures S2 and S3). Whole-brain analysis revealed a comparable projection pattern from the SNr in VGAT-Cre and PV-Cre mice (Figures S2L and S2M).

Across the 42 downstream targets of the SNr in the diencephalon and brain stem, the density of SNr bouton innervation spans a continuous range over more than one and a half orders of magnitude (Figure 2A, left). When we account for the volume of downstream structures (Figure 2A, center), the total SNr bouton output is enriched in a limited set of structures, including the VM thalamus, PPN, and dorsal *zona incerta*—6.1%, 5.8%, and 4.6% of the total SNr output, respectively. Nearly two-thirds of the output from the SNr targets the brain stem reticular formations and the colliculi (33.9% across the MidRF, PNo, and PcRT/IRT and 30.9% across the central superior colliculus [CSC], lateral superior colliculus [LSC], medial superior colliculus [MSC], and inferior colliculus [IC]), whereas the remaining 32 structures each receive less than 2% of the total bouton output (Figures 2A, right, and 2D).

A quantitative analysis shows that the probability density function for the axonal density is roughly exponentially distributed

Figure 1. Brain-wide axonal projection pattern from the SNr

(A) Schematic of the potential global architecture, where intermixed SNr neurons project to all target regions with equal probability but not necessarily equal axonal density.

(B) Schematic of the potential regionally divided architecture, where different pools of neurons project to each target, and the projection pools are spatially segregated.

(C) Representative *in situ* hybridization of Pvalb (red) and Slc32a1 (green) mRNA in the SNr (left) and proportion of Pvalb+ GABAergic and Th+ dopaminergic neurons in the SNr (right, 39 sections). Error bars, SEM.

(D) Anterograde tracing of SNr projections labeled with AAV-DJ-hSyn-FLEX-mGFP-2A-synaptophysin-mRuby injected into the SNr of a PV-Cre mouse.

(E–K) Whole-brain, high-resolution (0.325 μm/pixel) slide scanning of SNr axons (green) and boutons (red) demonstrates projections to (E–G) motor and intralaminar/midline thalamic, subthalamic, and incertal nuclei, (H1–H3) domains of the SC, and (H4 and I–K) diverse premotor brain stem regions, including the MidRF, PNo, and Med.

(L) Spatial distribution of synaptophysin-mRuby-labeled SNr boutons in 3D reconstructions of the diencephalon and general divisions of the brain stem.

See also Figure S1.

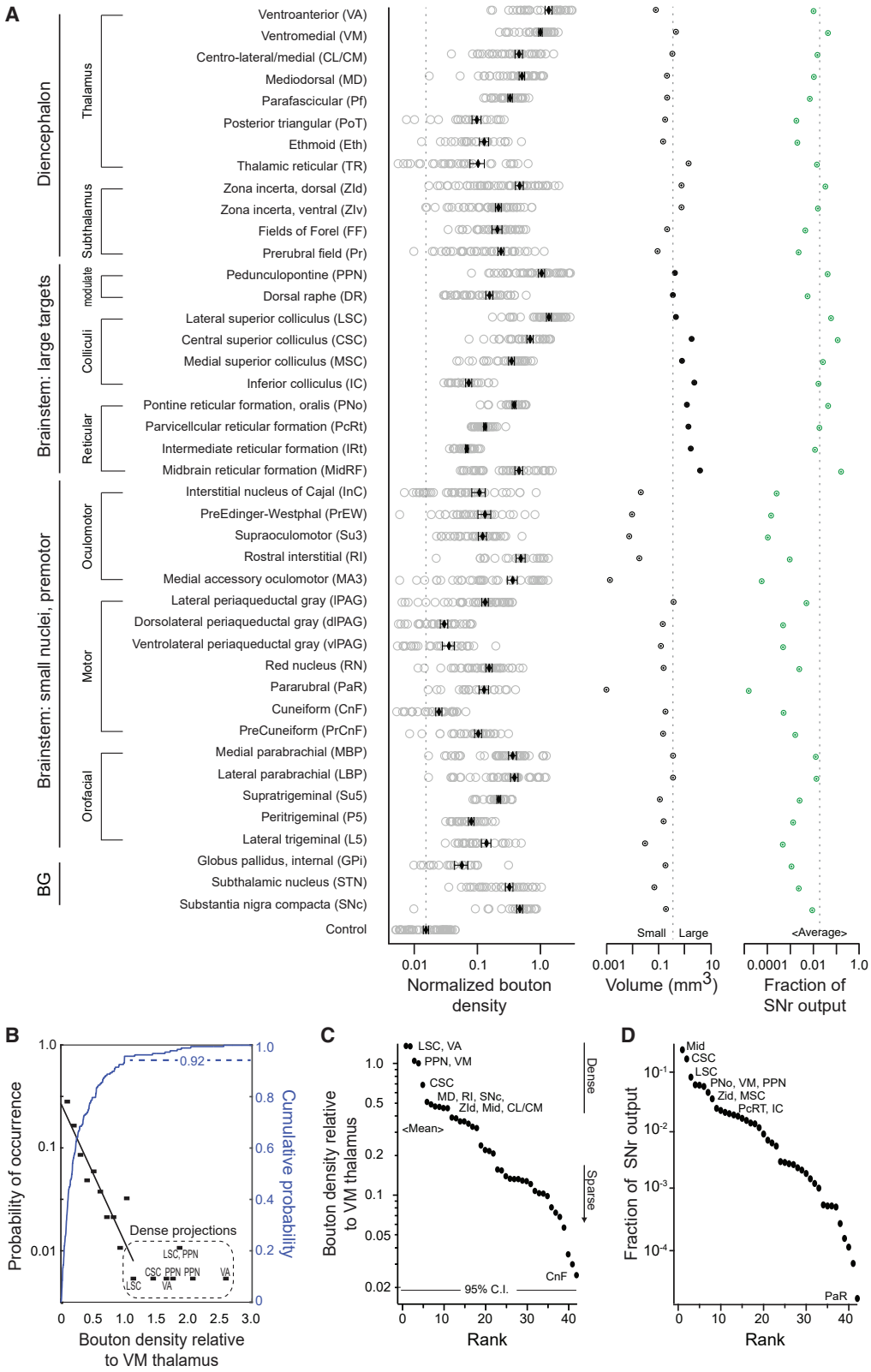

(legend on next page)

across the major fraction of SNr targets until a plateau is reached (black scale, Figure 2B). The plateau corresponds to innervation of the densest targets. These targets comprise the well-established SNr targets (i.e., the VA and VM motor thalamus, PPN, and superior colliculus; Figures 2B and 2C); however, the vast majority of total SNr output spans areas outside of these targets (Figure 2D). The SNr targets an expansive and diverse set of anatomical substrates (Figures 2A, S2, and S3) through a continuum of dense-to-sparse projections (Figures 2A–2C). The major fraction of total output is concentrated in several large brain stem regions and, to a lesser extent, the *zona incerta* and motor thalamus (Figure 2D).

SNr neurons exhibit heterogeneous electrophysiological properties

Do SNr neurons have diverse intrinsic electrophysiological properties? The spiking responses of SNr neurons during behavior include increases and decreases in rate across broad ranges and variable durations (Gulley et al., 1999; Hikosaka and Wurtz, 1983; Jin and Costa, 2010). It is unknown whether this heterogeneity arises from different synaptic inputs through afferents or network interactions or a spectrum of electrophysiological properties intrinsic to SNr neurons. To assess the firing properties across SNr neurons, we first performed whole-cell patch-clamp recordings from SNr neurons in young adult mouse midbrain slices. Across the population, neurons (120 cells from 14 mice) exhibited a capacity for highly regular and tonic firing (Atherton and Bevan, 2005) (Figure 3A), rapid action potential kinetics (Figure 3B), and sustained, high-rate activity (Figure 3C). Most critical, SNr firing responses to depolarizing inputs are highly linear ($R^2 = 0.99 \pm 0.01$) (Figure 3C). The limited adaptation and linearity of the neuronal input-output relation is consistent with open-loop drive for a motor system (Aström and Murray, 2008), akin to linear neuronal and synaptic properties common in brain stem sensorimotor networks (Kolkman et al., 2011; McElvain et al., 2010) and unlike forebrain projection neurons. In contrast, responses to hyperpolarizing inputs are non-linear, and the capacity for post-inhibitory rebound firing varied significantly across the population (Figure 3D). The broad continuum found for each electrophysiological property (e.g., gain, firing rate ranges, and rebound kinetics) can differentially tune the firing capabilities of individual neurons in the SNr.

Distinct SNr subpopulations project to large brain stem effector regions

We next ascertained how the remarkable diversity of SNr cellular properties maps onto specific anatomical projection targets. The large brain stem targets of the SNr have been implicated in disparate behavioral functions, involving distinct body parts and muscle groups. Do distinct SNr neuron pools that project to different downstream effector regions have specialized electrophysiological properties? To test this possibility, we first injected each of the large brainstem regions (Figure 2A, center) with a fluorescent retrograde tracer and targeted whole-cell recordings to labeled projection neurons (Figure 4A). In the hindbrain, the large SNr targets are the Med (i.e., subdivisions PcRT/IRT), PNo, and DR (Figures 1I–1K). Large midbrain targets of the SNr are the IC and superior colliculus (SC) (Figure 1H). Three medial-lateral domains of the SC were treated separately in light of the spatial specificity of their visual and somatosensory inputs (Comoli et al., 2012; Dräger and Hubel, 1976) and topographical organization of collicular output projections from the LSC, CSC, and MSC (Dean et al., 1988; Redgrave et al., 1987a, b; Wang and Redgrave, 1997; Yasui et al., 1994; Figure S4).

We find that SNr neurons projecting to different large brain stem regions exhibit notable electrophysiological specializations (4–7 mice per target; see Figure S5 for injection parameters). Projections to the colliculi arise from neuronal pools with different signaling capabilities. Neurons that project to the LSC and CSC have a relatively rapid rise and fall of their action potential, as seen by plotting its derivative, dV/dt, versus the amplitude of the transmembrane potential, V (Figure 4B, left blue and green curves), and high spontaneous and maximum firing ranges (Figures 4C and 4D). In contrast, projections to the MSC and IC arise from relatively slower neuronal pools (Figures 4B–4D). SNr projections to hindbrain targets exhibit electrophysiological differences such that projections to the PNo and Med exhibit a rapid rise and fall to their action potential and high spike rates (Figures 4B–4D). In contrast, neurons projecting to the DR exhibit slow action potentials, low firing rates, and long time constants and comprise the slowest projection population in the SNr (Figures 4B–4D). Rather than spanning the full diversity in the SNr, the intrinsic parameters of each of these projection populations span a restricted range (Figures 4D, S5C, and S6). This shows that different projection populations have specific functional properties.

Neurons in the SNr that project to brain stem areas span a range of post-inhibitory rebound firing capabilities. Robust non-linear rebound firing responses to hyperpolarization are greatest in neurons projecting to the Med and IC, which exhibited bursting up to hundreds of spikes per second and averaged 69 ± 15 Hz and 58 ± 11 Hz, respectively (Figure 4E). In contrast, transient and sustained rebound firing of other projection populations is modest, and neurons projecting to the DR exhibit the lowest capacity for rebound (Figures 4E). Thus, rather than each projection population spanning the full continuum of

Figure 2. Density and distribution of SNr terminal fields in diverse thalamus and brain stem regions

(A) Left: Average bouton density in each of 42 identified target structures, normalized to the density in the VM motor thalamus (5 mice). Center: target structure volumes. Right: proportion of total SNr bouton output. Error bars, SEM.

(B) Probability density function (black) and cumulative probability (blue) of bouton density across all targets relative to the VM thalamus.

(C) Rank-ordered bouton densities. The most densely innervated targets are the motor thalamus (VA/VM), pedunculopontine nucleus (PPN), central superior colliculus (CSC), and lateral superior colliculus (LSC), and the weakest is the cuneiform nucleus (CnF). The gray line is the 95% confidence interval of background autofluorescence.

(D) Rank order of the proportion of SNr bouton output per structure, calculated from mean bouton density and structure volume.

See also Figures S2 and S3.

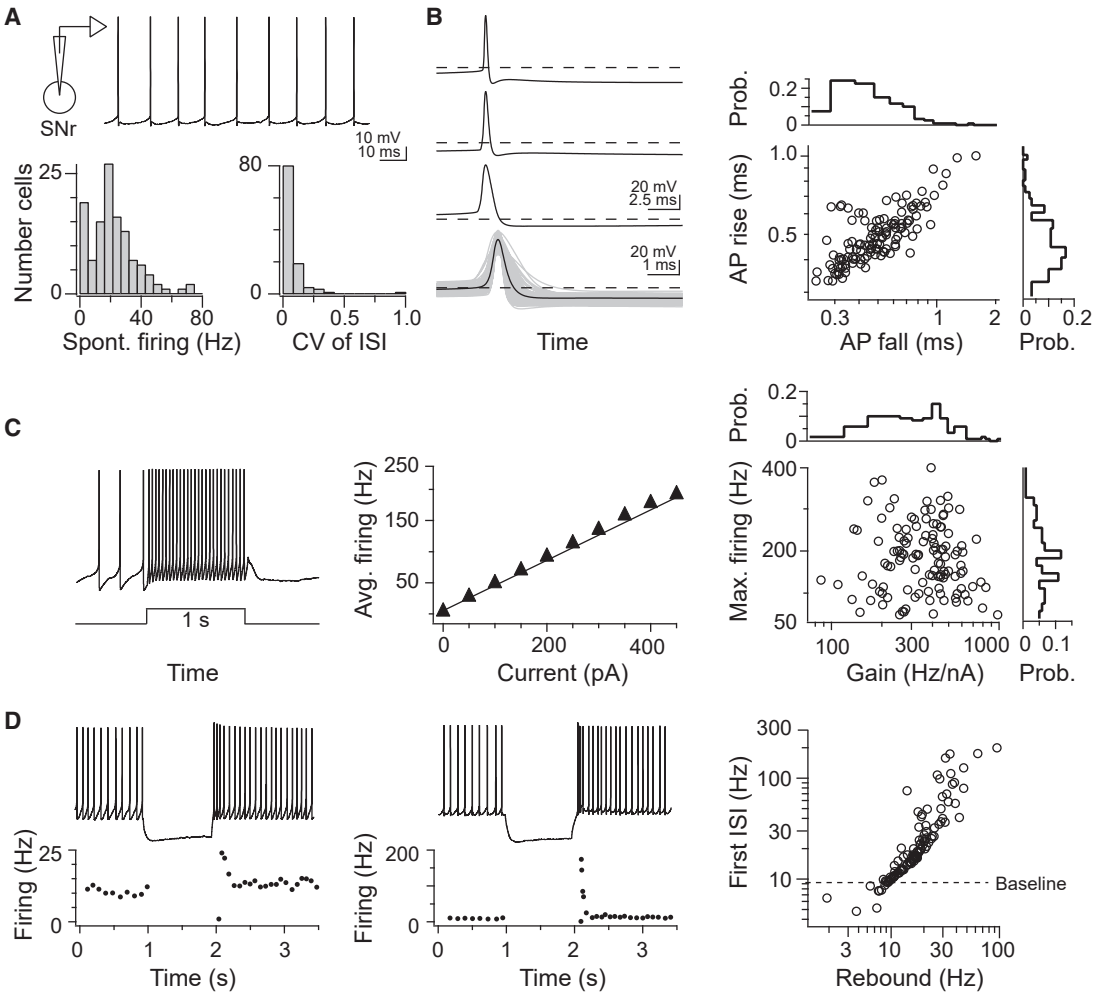

Figure 3. Continuum of intrinsic electrophysiological properties in the SNr

Whole-cell patch-clamp recordings of SNr neurons *in vitro* (120 cells) were performed.

(A) Top: representative current-clamp trace of spontaneous SNr firing. Bottom: histograms of spontaneous firing rates (mean = 21 ± 15 Hz) and inter-spike interval (CV = 0.1 ± 0.1) in the SNr.

(B) Left: three example action potential waveforms and the mean waveform (bottom) overlaid with all recorded waveforms (gray). Right: action potential waveforms in SNr neurons are characterized by highly correlated rise and fall durations.

(C) Left: 1-s depolarizing current step injected into an SNr neuron evokes sustained higher firing. Center: evoked firing rates increase as a linear function of current over a wide range. Right: across the SNr populations, the capacity to sustain fast firing and the sensitivity to current inputs (neuronal gain) varied over a more than 10-fold range, but the mean firing responses increased linearly to depolarization in all neurons (R^2 = 0.99 ± 0.01).

(D) Non-linear firing responses to hyperpolarizing inputs in two neurons that display (left) modest and (center) robust post-inhibitory rebound firing from a 10-Hz baseline rate. The SNr population displays heterogeneous responses to hyperpolarization, quantified as the first post-inhibitory instantaneous rate and the rate sustained over 200 ms.

electrophysiological properties, projections to large brain stem areas arise from subpopulations of SNr neurons whose properties are tuned differentially.

SNr-brain stem projection neurons cluster spatially in the SNr (Figure 4F) and form a spatial continuum of electrophysiological properties (Figure S6C). Projection neurons that exhibit slower active and passive properties are concentrated in the medial portion of the nucleus (Figure S6C), which overlaps with terminal fields from associative striatal regions. Slow neurons are additionally located in a small cluster at the dorsal-most extreme portion of the SNr, which extends in the *substantia nigra lateralis* (SNl) and overlaps with terminal fields from the auditory striatum (Deniau et al., 1996; Figure 4F). In contrast, rapidly responding projection neurons occupy the lateral half of the SNr (Figures 4F and S6), where sensorimotor striatal afferents terminate (Deniau et al., 1996), positioning different SNr projection neurons to differentially process striatal signals.

Broadly tuned SNr projections to thalamic nuclei and the PPN

We next targeted neurons that project to major thalamic nuclei and the PPN (Figure 5) for whole-cell recordings. SNr neurons

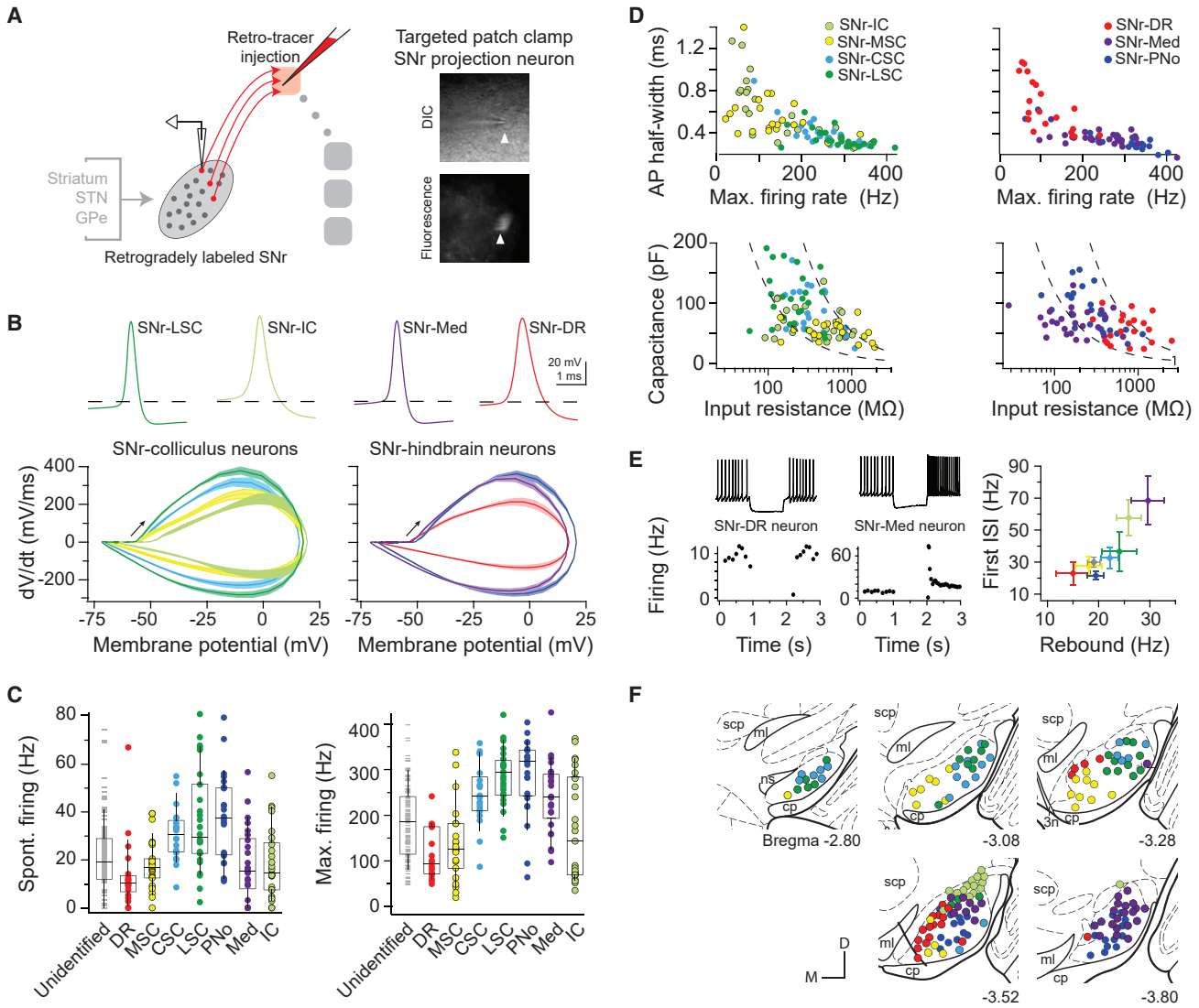

Figure 4. Specialized SNr subpopulations innervate large, functionally distinct brain stem regions

(A) SNr projection neurons were labeled via retrograde tracer injection into a single downstream brain stem region in each animal, and whole-cell recordings were targeted to fluorescent, retrogradely labeled SNr neurons. 4–7 mice per each target.

(B) Average action potential waveforms and phase-plot kinetics of identified projection neurons. Left: SNr-LSC (green), SNr-CSC (light blue), SNr-MSC (yellow), and SNr-IC (light green) neurons. Right: SNr-PNo (dark blue), SNr-Med (purple), and SNr-DR (red) neurons.

(C) Range of spontaneous and maximum firing rates across projection neuron pools and in randomly targeted SNr neurons (gray). Boxplots show quartiles and median (boxes) and 10%–90% range (whiskers).

(D) Active (top) and passive (bottom) properties of projection neurons fall on a continuum.

(E) SNr neurons projecting to brain stem areas span a range of post-inhibitory rebound firing capabilities. Left: example neuron projecting to the dorsal raphe (DR) exhibited no increase in firing in response to hyperpolarization, whereas an example neuron projecting to the medullary reticular formation (Med) exhibited robust rebound firing capabilities. Right: average transient and sustained rebound firing rates of each brain stem projection population. Error bars, SEM.

(F) Topographical distributions of SNr projection neuron recording locations, registered to five atlas coronal sections.

See also Figures S4–S6.

projecting to the VA, MD, or Pf thalamus each displayed the full diversity of firing properties observed across SNr neurons (Figures 5A–5C and S5C). Similarly, SNr neurons projecting to the PPN were tuned broadly with heterogeneous properties (Figures 5A–5C) and lacked statistically significant differences from randomly selected SNr neurons (Figure 5E). In addition to a lack of specialized intrinsic properties, SNr-thalamus and SNr-PPN projection neurons were distributed throughout the SNr (Figure 5D). SNr populations labeled retrogradely from several brain stem regions exhibit intrinsic electrophysiological properties that differ statistically from randomly targeted SNr neurons (Figure 5E), indicating that each of these regions is dominated by output from a subpopulation of SNr neurons. In contrast, SNr populations labeled from the PPN and thalamic nuclei

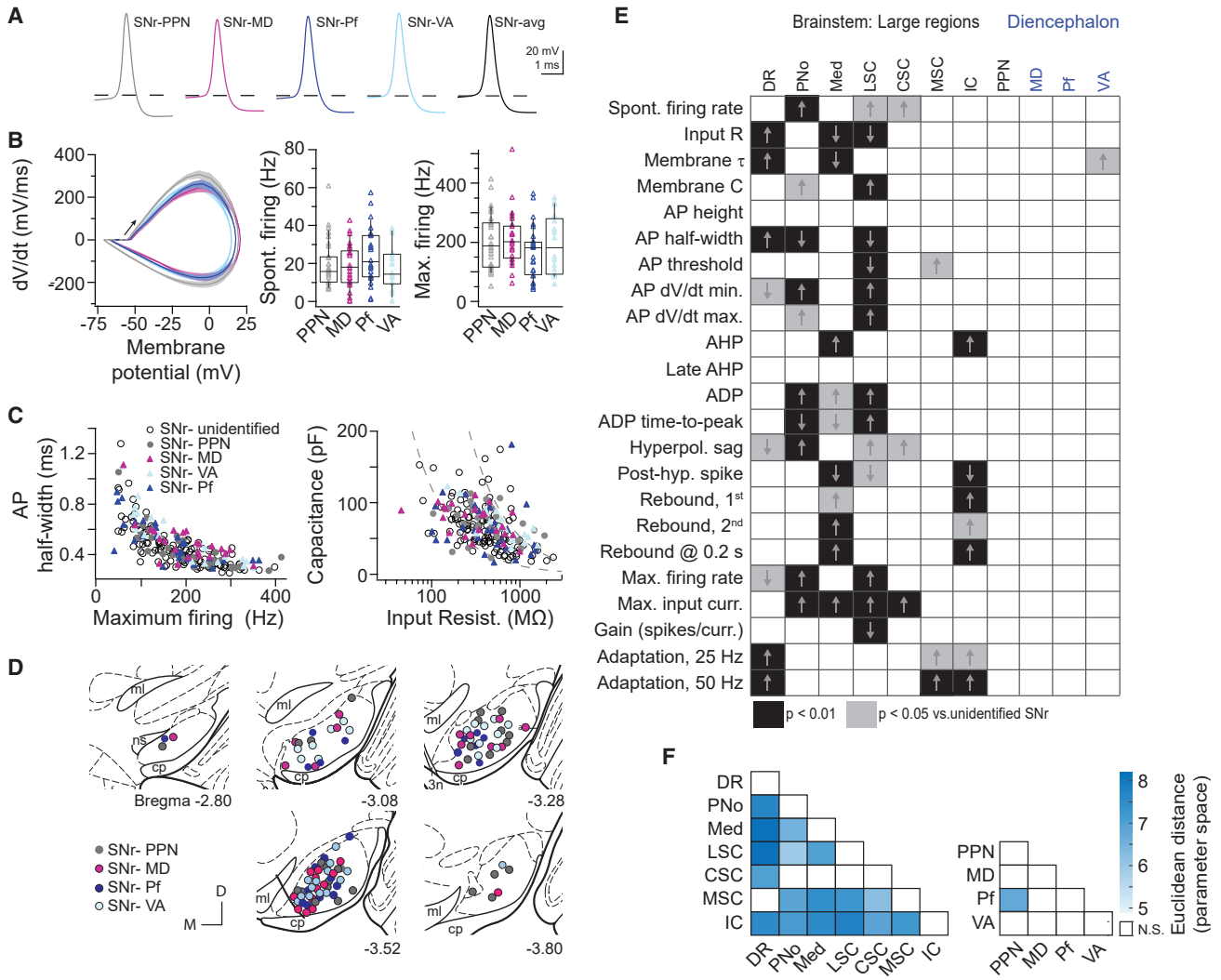

Figure 5. SNr neurons projecting to the PPN and thalamic nuclei are broadly distributed in the SNr and electrophysiologically heterogeneous

(A) Average action potential waveforms of SNr neurons labeled via retrograde tracer injection into the pedunculopontine nucleus (PPN, gray), mediodorsal (MD; magenta), parafascicular (Pf; dark blue), or ventroanterior (VA; light blue) nucleus; 3–5 mice per each target.

(B) Action potential kinetics (left) and range of spontaneous and maximum firing rates of labeled projection neurons (right). Boxplots show quartiles and median (boxes) and 10%–90% range (whiskers).

(C) Distributions of projection neuronal populations overlaid with the full diversity of SNr electrophysiological properties (open circles).

(D) Broad topographical distributions of SNr projection neuron recording locations, registered to five atlas coronal sections.

(E) Chart of statistical significance of (rows) intrinsic properties in (columns) retrogradely labeled populations compared with unlabeled SNr neurons (403 neurons across 72 mice); Kruskal-Wallis and Dunn post hoc tests for significant differences at the $p < 0.05$ (gray) and $p < 0.01$ (black) levels. Arrows indicate whether the value was larger or smaller in the retrogradely labeled population.

(F) Quantification of pairwise differences between composite electrophysiological properties in retrogradely labeled SNr populations. Heatmap of Euclidean distances computed from *Z*-scored electrophysiological properties; intensity corresponds to the distance. White, not statistically different, $p < 0.01$.

See also Figures S5 and S6.

exhibit no highly significant differences (Figure 5E). To assess pairwise differences between populations, we additionally calculated the Euclidean distance between all *Z*-scored intrinsic parameters and resampled the datasets to assess significance. The populations of SNr neuron projecting to brain stem targets differed extensively from each other, in contrast to SNr-thalamus and PPN projection neurons (Figure 5F). Thus, projections to the thalamus and PPN arise from broadly tuned projection pools in the SNr, in contrast to the specialized features of SNr projections to most large brain stem areas.

Collateral organization of SNr projections is broad and specific

The heterogeneity of SNr neurons that project to the PPN and thalamic nuclei could arise from two possible circuit configurations. First, each of these projections could arise from a distinct,

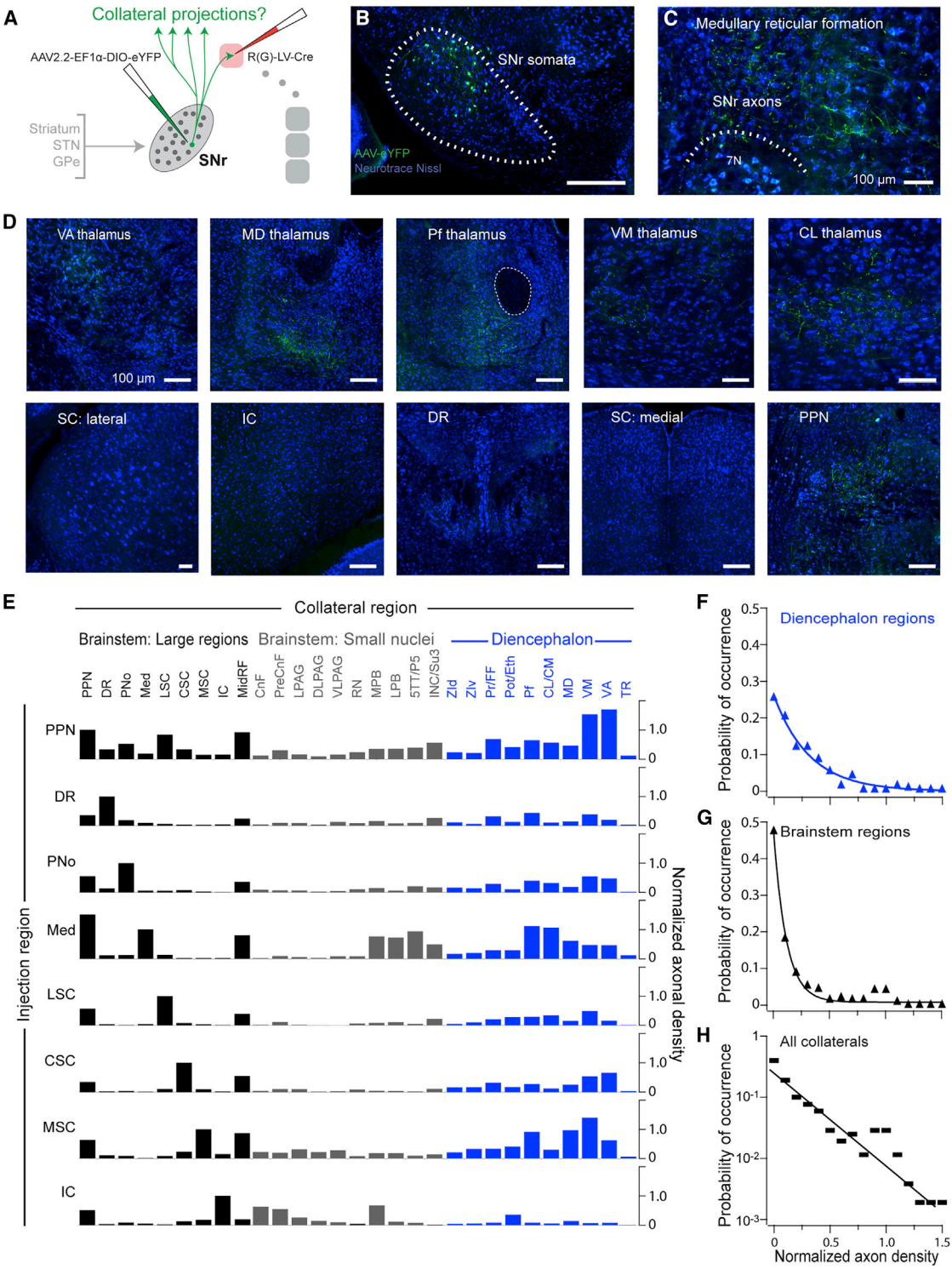

Figure 6. Broad and specific collateralization of SNr outputs demonstrated by projection-based intersectional viral mapping

(A) Schematic of the intersectional viral strategy to map SNr collateral projections across the whole brain. Injections of a retrograde lentivirus expressing Cre (RV(G)-LV-Cre) were made to a single downstream target. A Cre-dependent AAV expressing eYFP was injected into the SNr, and the whole brain was serially sectioned and imaged for axon collaterals.

(B) Example injection site showing eYFP+ neurons in the SNr following injections of a retrograde Cre-expressing lentivirus into the Med and the Cre-dependent AAV expressing eYFP into the SNr.

(legend continued on next page)

broadly tuned, and spatially distributed population, or, second, these projections could arise from converging collaterals of the diverse SNr projection populations that target large brain stem regions (Figure 4). Consistent with the second possibility, SNr neurons that project to the PPN and thalamic nuclei exhibit topographical organization in their electrophysiological properties so that thalamus-projecting neurons in the lateral SNr are larger, fire at faster rates, and have faster membrane time constants (Figure S6), comparable with SNr neurons that project to large brain stem targets. The presence of collateral projections to the thalamus, SC, and PPN has been assayed previously with dual chemical tracer injection and antidromic stimulation, yet with conflicting results (Anderson and Yoshida, 1977; Beckstead and Frankfurter, 1982; Deniau et al., 1977; Parent et al., 1983). We utilized an intersectional virus mapping strategy to unambiguously determine the complete pattern of SNr collateralization (Figure 6A). To label collaterals throughout the brain, a rabies-pseudotyped lentivirus expressing Cre was injected into a single downstream target in each mouse. This virus retrogradely infected SNr projection populations, and a Cre-dependent AAV expressing eYFP (AAV2.2-Ef1a-DIO-eYFP) was targeted to the SNr to label projection neurons and their terminals with eYFP (Figures 6B–6D). The analysis of serial sections across the whole brain was used to assess whether eYFP+ projection neurons emitted axonal collaterals in additional regions.

We injected the retrograde lentivirus into each of eight volumetrically large brain stem regions (Figure 6E; n = 18 mice). These encompass regions that receive a disproportionally large fraction of total SNr output (Figure 2D) and whose projection neurons from the SNr exhibit differing electrophysiological properties (Figure 4). From each population of SNr neurons projecting to large brain stem areas, axons collaterals were observed in diverse additional targets (Figures 6E and S7). SNr projection neurons labeled retrogradely from the DR, PNo, Med, LSC, CSC, and MSC each collateralize densely to diencephalic nuclei (labels in blue, Figure 6E; see also Figures S7 and S8), the PPN, and the MidRF but sparsely or not at all to each other. Additional collateral projections target a broad range of smaller brain stem sensorimotor nuclei (labels in gray, Figure 6E). As an exception, nigral projections to the IC, whose somata span the dorsal SNr and SNl, do not collateralize extensively to the diencephalon but do collateralize to the PPN, MidRF, and several premotor brain stem nuclei. The strength and probability of collaterals to diencephalic targets (Figure 6F) is distributed more uniformly than those to brain stem targets (Figure 6G). Last, at a statistical level, we see that the strength of collaterals is distributed exponentially over a 200-fold range (Figure 6H), on the same order of magnitude as seen in the initial anterograde mapping (Figure 2B).

To verify that the PPN is indeed a broad collateral hub of the SNr, the PPN was additionally targeted with the retrograde lentivirus. Consistent with data showing broad collaterals to the PPN, SNr neurons labeled retrogradely from the PPN collateralized to all other SNr targets (Figures 6E, top).

Although the SNr predominantly contains GABAergic neurons, a small population of dopaminergic neurons is also present (4.2% ± 0.1% of neurons in the SNr express tyrosine hydroxylase; Figure S1; González-Hernández and Rodríguez, 2000), and evidence suggests that a fraction of putatively dopaminergic neurons in the SNr project to the thalamus and PPN (Cebrián and Prensa, 2010; Prensa and Parent, 2001). To verify that the collaterals mapped from the SNr arise specifically from GABAergic neurons, we performed additional collateral tracing restricted to GABAergic SNr neurons. In particular, a Cre-dependent retrograde lentivirus that expresses Flp (RG-EIAV-DIO-FLP) was injected into a subset of downstream targets, and a Flp-dependent AAV (AAV2.2-fDIO-eYFP) was targeted to the SNr in PV-Cre mice (Figure S7C). In this genetically and projection-based intersectional tracing strategy, eYFP+ collateral axons displayed a pattern comparable with those in wild-type mice, including collateral fibers in the VM and Pf thalamus and the PPN (Figures S7D and S7E).

These data indicate that SNr neurons emit a broad but specific pattern of axonal collateralization, with diencephalic regions receiving broader collateral input than brain stem regions (Figure 6E–6G). This indicates that the SNr targets the diencephalon in a relatively diffuse manner compared with brain stem nuclei. In addition to diverse nuclei in the thalamus, two downstream brain stem targets also form common hubs for collateral inputs: the PPN and MidRF. Notably, converging collaterals in common targets of the SNr underlie their exceptionally dense bouton innervation (Figure 2C).

Parallel SNr projections to the thalamus exhibit topographical organization

The cerebral cortex and striatum contain highly organized subdomains (Gabbott et al., 2005; Nambu, 2011; Svoboda and Li, 2018), which questions how broad SNr collateralization to thalamic nuclei supports behavioral or functional specificity within SNr-thalamocortical and SNr-thalamostriatal feedback loops. Do ascending SNr projections intermix fully in thalamic nuclei or, alternatively, do they target specific nucleus subdomains? We performed automated reconstructions of SNr axon positions in the diencephalon to ascertain fine-scale topography in thalamic nuclei. Serial sections of collateral axon locations were stacked and aligned to corresponding atlas sections (Franklin and Paxinos, 2013), and contour density was computed relative to anatomical landmarks (Figure 7). Rather than

(C) Anterogradely labeled eYFP+ SNr axons at the lentivirus injection site in the medulla.
(D) Anterogradely labeled eYFP+ axon collaterals from SNr-medulla-projecting neurons are distributed throughout diverse thalamic nuclei (top) and in the PPN (bottom right) but not in other large brain stem regions.
(E) Collateral projections from different SNr projection populations. Axonal density is quantified in each downstream region (left to right) following labeling of specific SNr projection populations via injection of a retrograde lentivirus expressing Cre to large brain stem regions (left) and AAV complementation in the SNr. Axonal density was normalized to that in the lentivirus-targeted region. See also Figure S7A.
(F) Compendium of collateral innervation density across diencephalic targets in all experiments.
(G) Compendium of collateral innervation density across brain stem targets.
(H) Occurrence of collateral innervation density across all targets; the line is an exponential with a decay constant of 0.27.
See also Figure S7.

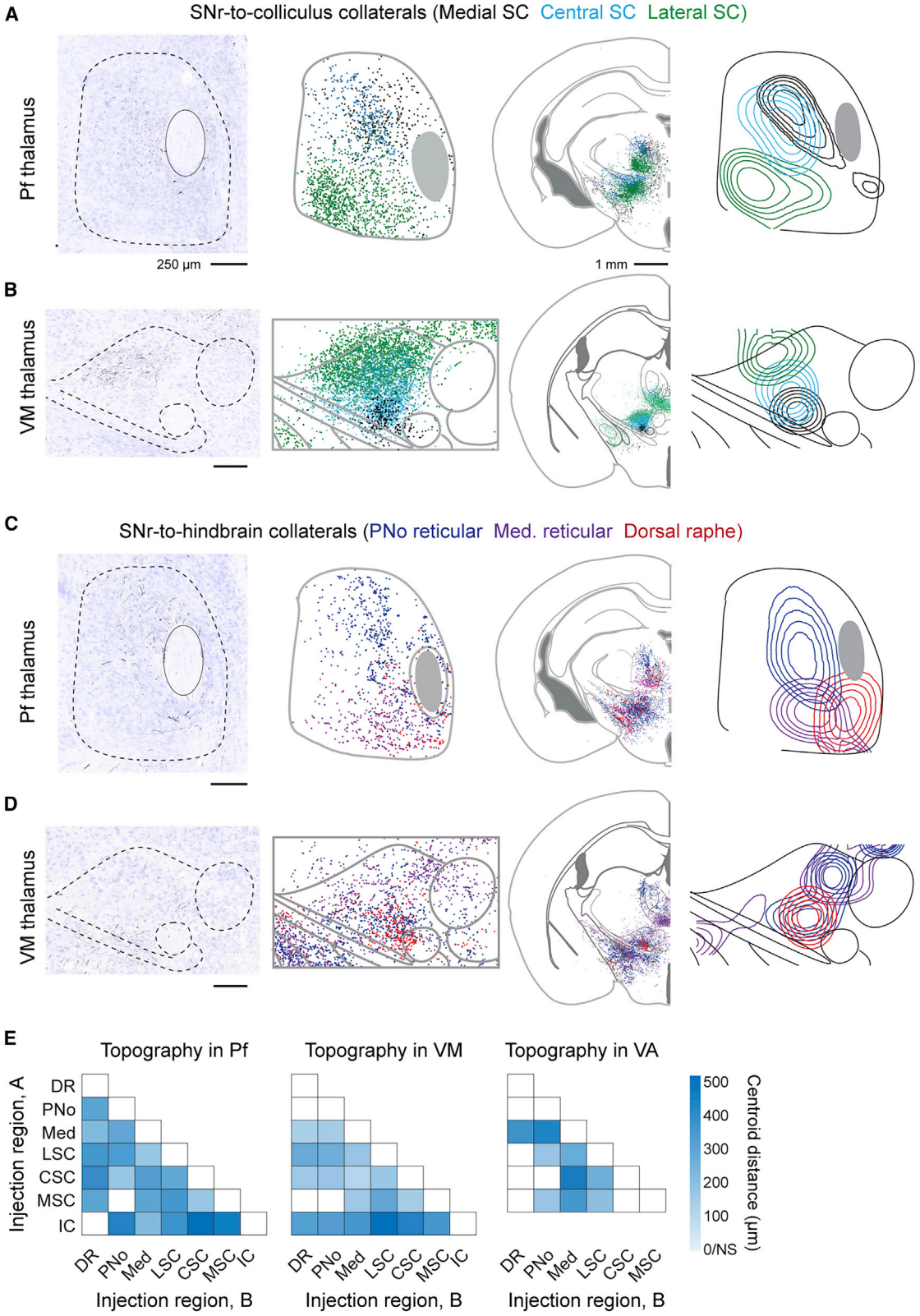

(legend on next page)

spanning entire nuclei, axonal collateral fields of each SNr-brain stem projection pool target restricted subdomains. In the Pf and VM thalamus, collaterals from SNr-colliculus projections targeted relatively lateral domains of the nuclei (Figures 7A and 7B), whereas collateral SNr-hindbrain projections targeted relatively medial domains (Figures 7C and 7D).

To quantify the topography of SNr projections in thalamus, we measured the Euclidean distances between axonal terminal field centroids (Figure 7E). In the Pf and VM thalamus, pairwise centroid distance measurements demonstrate that collateral axon fields of most populations were offset significantly (Figure 7E; $p < 0.01$) relative to the replicates in each population (Figures S8A and S8B). Topography was assessed further by measuring the extent of overlap between each collateral terminal field using the weighted Jaccard pairwise similarity index (Jaccard, 1912), J_{AB} (Figure S8D), where $J_{AB} = 0$ indicates a lack of overlap, and $J_{AB} = 1$ indicates complete overlap. Across the Pf, VM, and VA motor thalamus, the J_{AB} of collateral overlap was small, 0.24 ± 0.12 (mean ± SD) and significant (Figures S8D and S8E). Thus, rather than intermixing, collateral projections from distinct SNr neuronal populations primarily tile the thalamic nuclei, comparable with the fine-scale topography of thalamic projections to the cortex and striatum (Aldes, 1988; Cicirata et al., 1986; Mandelbaum et al., 2019; Smith et al., 2004) and consistent with segregated feedback loops.

The topography of SNr terminals in MD, CL/CM, and VA additionally shows spatial biases, although with a more complex pattern (Figure S8). Notably, although nigral projections to the IC do not collateralize extensively to the VM or Pf thalamus proper, spatial mapping of their axonal projections reveals sparse collateral projections to small domains on the periphery of the VM and Pf thalamus (Figures S8A–S8C).

Topographically organized subdivisions of SNr

To assess the three-dimensional organization of projection pools in the SNr, we reconstructed the positions of retrogradely labeled SNr projection neurons and aligned each experiment with a common reference frame (Figure 8A). Projection neuron populations are highly organized in the SNr. Neurons projecting to the IC (SNr-IC), MSC (SNr-MSC), CSC (SNr-CSC), and LSC (SNr-LSC) are located relatively rostral and lateral of neurons projecting to the DR (SNr-DR), PNo (SNr-PNo), and Med (SNr-Med). Thus, SNr neurons that project to the colliculus spatially segregate from those that project to the hindbrain along a rostral-caudal division. Among SNr-colliculus neurons, those projecting to the IC are most lateral/dorsal, whereas projections along the medial-to-lateral axis of the SC arise from neurons spanning the medial-to-lateral extent of the rostral SNr. Along SNr-hindbrain neurons, SNr-DR, SNr-PNo, and SNr-Med neurons are situated along a medial-to-lateral axis in the caudal SNr. In addition to their topographically organized axon project patterns, projection neurons in the SNr are positioned to operate as parallel, separable output modules.

DISCUSSION

This study demonstrates direct and extensive connections from basal ganglia to diverse components of the thalamocortical and brain stem motor systems. Rather than a single monolithic output, the SNr contains distinct projection neuronal pools that are electrophysiologically specialized and topographically organized and differentially target brain stem effector circuits. Each projection pool emits ascending, spatially organized collateral branches to several thalamic nuclei and broadly collateralizes to the PPN and MidRF. These findings demonstrate that the well-known closed-loop architecture of basal ganglia-thalamocortical circuits overlaps with broad descending projections to brain stem premotor and modulatory networks. This work establishes a framework of basal ganglia output via discrete SNr modules and their connections to the broader motor system.

Pattern of mesoscopic connectivity

Our anterograde tracing and analysis demonstrate that neurons in the SNr project to an unexpectedly large number of targets. The broad distribution of axonal density to collateral regions demonstrates that basal ganglia outputs are not organized in a one-to-all (Figure 1A) or one-to-one (Figure 1B) circuit architecture. Rather, output projections arise from separable pools of neurons that broadcast to a discrete set of targets in the brain stem (Figure 4 and 6). These targets are large volumetric regions; i.e., the central (CSC), medial (MSC), and lateral (LSC) domains of the SC, IC, DR, PNo, and Med (Figure 2A). Each SNr projection pool sends a copy of its output to a set of common collateral targets, which include the PPN and MidRF in the brain stem and the motor and intralaminar/midline thalamus and ZI in the diencephalon (Figures 6E and 8B). Importantly, whether every neuron in each projection pool follows the mesoscopic pattern or, alternatively, targets a further restricted set of targets remains to be determined.

Circuit architecture: Descending and ascending connections to the broader motor system

Axonal projections from the SNr to large domains of the reticular formation and premotor nuclei throughout the midbrain, pons,

Figure 7. Parallel ascending collaterals target topographically distinct domains in the intralaminar and motor thalamus

(A and B) SNr neurons that project to the MSC (black dots and contours), CSC (light blue), and LSC (green) send collateral projections to the Pf (A) and ventromedial (VM; B) thalamus. The left panels are single-section examples of axon collaterals arising from neurons that project to the central (A) and lateral (B) SC. Center and right: composite overlay (center) and isodensity contour plots (right) of collateral locations.

(C and D) SNr neurons that project to the hindbrain nuclei, including the PNo (deep blue), Med (purple), and DR nucleus (red), send collateral projections to the Pf (C) and VM (D) thalamus. The left panels show single-section examples of axon collaterals arising from neurons that project to the PNo (C) and DR nucleus (D). Center and right: composite overlay (center) and isodensity contour plots (right) of collateral locations.

(E) Heatmap of Euclidean distances between centroids of collateral axon terminal fields in the Pf, VM, and VA thalamus. Distances were calculated pairwise for each collateral population labeled from SNr-brain stem targets, labeled A and B. The intensity corresponds to the distance. White, not statistically different, $p < 0.01$.

See also Figure S8.

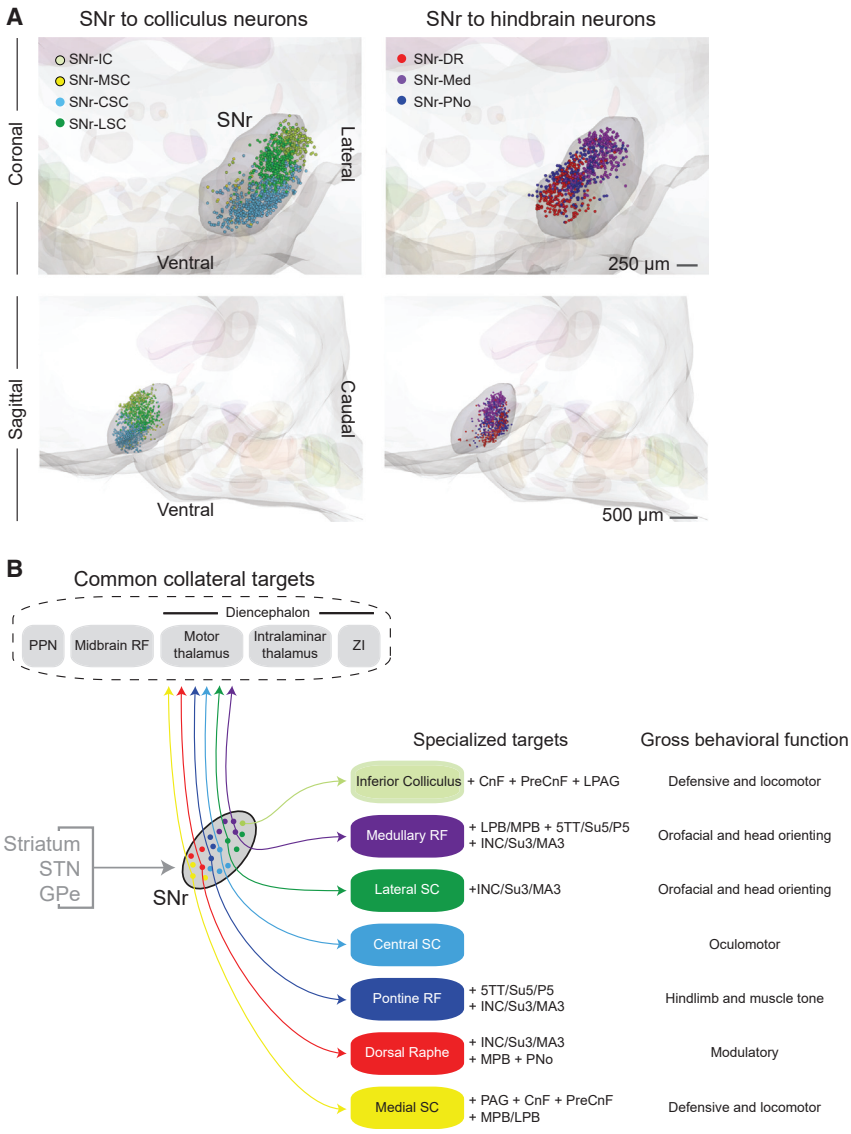

Figure 8. SNr subdivisions contain topographically organized projection populations

(A) Three-dimensional reconstructions of SNr projection neurons labeled by retrograde viral tracers, aligned to a common brain stem atlas. The composite displays the relative position of SNr neurons projecting to midbrain (left) and hindbrain targets (right). Also shown are coronal (top) and sagittal (bottom) views of neurons projecting to the IC (SNr-IC; light green), MSC (SNr-MSC; yellow), CSC (SNr-CSC; light blue), LSC (SNr-LSC; green), DR (SNr-DR; red), PNo (SNr-PNo; dark blue), and Med (SNr-Med; purple).

(B) Summary of SNr output pathways demonstrating unique and common targets of distinct SNr projection populations. Each SNr population projects to large, functionally distinct brain stem regions and collateralizes to small brain stem nuclei and a set of common target regions. All projection populations demonstrate a distinct one-to-many projection pattern.

and hindbrain (Figures 2, S2, and S3) reveal that basal ganglia have extensive and relatively direct access to low-level motor circuitry. The SNr targets many regions that project directly to the spinal cord, including the fields of Forel, ZI, medial Pf thalamic nucleus, red nucleus, interstitial nucleus of Cajal, SC, PPN, PAG, precuneiform nucleus, parabrachial nuclei, and distinct regions of the reticular formation (Liang et al., 2011); many SNr target regions additionally contain premotor neurons for orofacial, vocal, and oculomotor nuclei (Büttner-Ennever, 2006; Jürgens, 2002; McElvain et al., 2018; Stanek et al., 2014). Nearly all brain stem regions downstream of the SNr (Figures 2, S2, and S3) additionally receive afferents from the cerebral cortex (Alloway et al., 2010; Jeong et al., 2016; Sesack et al., 1989) as well as the cerebellum, hypothalamus, and amygdala (Asanuma et al., 1983; Holstege, 1987; Hopkins and Holstege, 1978). Identifying the mechanisms by which brain stem motor circuits integrate higher-order signals will be essential for understanding the circuit basis of volitional movement and the consequences of output from basal ganglia (Arber and Costa, 2018; Chen et al., 2019).

Theories of basal ganglia function have largely emphasized thalamocortical feedback loops and the role of the cerebral cortex in mediating basal ganglia effects on motor preparation and control (Alexander et al., 1990; Haber and Calzavara, 2009). In contrast, several lines of evidence have focused on SNr projections to a limited number of brain stem targets, particularly the role of SNr neurons that project to the SC (Hikosaka, 2007a; Holmes et al., 2012; Rossi et al., 2016; Wang and Redgrave, 1997). However, the findings that SNr axons branch across several thalamic nuclei (Cebrián et al., 2005) and that these SNr-thalamus projections comprise aggregate collaterals of SNr-brain stem projection neurons (Figures 6, 7, and S8) establishes a principle of circuit organization by which SNr neurons concomitantly affect cortical and brain stem systems. Branching ascending-descending collateral projections might ensure coordinated gating of cortical and brain stem circuitry and are a practical consideration for interpretation of experiments in which SNr neurons are labeled retrogradely from a single target. Similar ascending-descending branched projections have been observed among the outputs of diverse structures that regulate behavior, including the hypothalamus, cerebellum, and brain stem reticular formations (Bentivoglio and Kuypers, 1982; Risold et al., 1997; Scheibel, 2011).

Topographical organization of basal ganglia connectivity

Basal ganglia exhibit topographically organized inputs to the striatum (Hintiryan et al., 2016; Parent and Hazrati, 1995; Lee

et al., 2020) and connections between the striatum and *substantia nigra* (Deniau et al., 1996; Gerfen et al., 1987; Nambu, 2011). Systematic mapping of SNr projection domains into a three-dimensional model (Figure 8A) shows that this subnuclear organization additionally extends to basal ganglia output projections to distinct brain stem areas. Thus, rather than operating as a generic hub, the SNr is anatomically posed to subserve functions of discrete basal ganglia module channels, as described for its oculomotor functions (Hikosaka et al., 2014).

Diverse projection neuron populations in the SNr collateralize broadly to thalamic nuclei (Figure 6). The lack of electrophysiological specialization of neurons projecting to thalamic nuclei (Figure 5) thus likely reflects that the organization of SNr-thalamus projections is on a particularly fine spatial scale (~100 μm) (Figures 7 and S8). This subnuclear organization of SNr axons appears to correspond to fine-scale subdivisions of projection neurons in the thalamus (Aldes, 1988; Berendse and Groenewegen, 1990; Cicirata et al., 1986; Mandelbaum et al., 2019; Smith et al., 2004), which together could underpin subcircuit-specific feedback to the cortex and the striatum. The thalamic nuclei targeted by the SNr additionally receive topographically organized inputs from the vast majority of newly and previously identified SNr brain stem targets (Krout et al., 2002). Future investigations are needed to determine whether the SNr might have the additional capacity to influence the thalamus via disynaptic brain stem-thalamus pathways.

Specificity of firing properties in the SNr

SNr projection neurons do not form a homogeneous population in terms of their electrophysiological properties (Figures 3, 4, and 5), and neurons that project to different targets also have significant differences in their intrinsic electrophysiological properties (Figures 4, 5E, and 5F). SNr projection populations form a continuum of fast-firing GABAergic neurons that span a broad range of active and passive properties (Figure 3). However, fine-tuning of intrinsic electrophysiological properties, including spontaneous and maximum firing characteristics, membrane leakiness, and time constants, differentiates SNr projection populations targeting distinct brain stem effector regions (Figures 5E and S6B). Neurons projecting to classic motor structures (i.e., the LSC, CSC, PNo, and Med) exhibit notably fast intrinsic properties, whereas neurons projecting to the neuromodulatory DR comprise the slowest population in the SNr (Figure 4). Across the SNr, projection neurons (Figure 8A) and electrophysiological properties are spatially organized along a medial-lateral gradient so that the lateral portion of the nucleus is capable of operating at higher rates with faster kinetics (Figure S6C). A corresponding medial-lateral gradient in the distribution of terminals from the associative and sensorimotor striatum (Deniau et al., 1996) suggests that the medial-lateral axis of electrophysiological specializations in the SNr is situated to differentially process outputs of distinct associative versus sensorimotor striatal domains.

All neurons in the SNr have highly linear gain (i.e., firing rate versus input current; Figure 3C), consistent with engineering expectations for motor control circuitry in the excitatory domain (Aström and Murray, 2008). In contrast, the restricted expression of non-linear rebound mechanisms (Figure 4E) alters the signaling capacity of different SNr populations in response to inhibitory inputs, including from the striatum and *globus pallidus*. In particular, neurons projecting to the Med and IC exhibit notable rebound firing (Figure 4E). In neurons that fire tonically, post-inhibitory rebound mechanisms could transform synaptic inhibition into post-synaptic burst firing and/or well-timed spiking, which is likely to differentiate the capacity of direct versus indirect pathway synaptic inputs in rebounding neurons. In contrast, non-rebounding neurons could more linearly integrate inhibitory and excitatory synaptic drives. During behavior, the only well-studied SNr projection, that to the oculomotor SC, generally disinhibits effector neurons via firing rate decreases (Hikosaka, 2007b); however, notable increases in SNr firing rates, driven by an unknown circuit mechanism, are commonly observed during diverse behaviors (Gulley et al., 1999; Jin and Costa, 2010). The diversity in SNr-intrinsic properties questions whether common disinhibition mechanisms apply to all SNr outputs, which operate across different firing rate ranges (Figures 4 and S5), or whether signaling mechanisms vary according to the circuit demands of downstream structures.

Behavioral implications

Many reflexive motor actions are mediated by circuits in which one-to-one projections mediate behavioral responses (Arber, 2012; Büttner-Ennever, 2006; McElvain et al., 2018). However, the broad collateralization of SNr projections (Figure 6) indicates that simple one-to-one motifs do not underlie basal ganglia circuit mechanisms. Similarly diffuse outputs characterize motor-cortical projections (Economo et al., 2018; Kita and Kita, 2012). The broad but specific collateralization pattern of SNr neurons (Figures 6E and 8B) might ensure coherent gating of related behavioral control circuit modules. For example, the SNr projection neurons that target orofacial regions in the Med collateralize to several small brain stem nuclei implicated in orofacial sensorimotor signaling (Su5, P5, L5, and parabrachial nuclei) and vertical head orientation (InC) (Fukushima, 1987; Kolta et al., 2010; Figures 6B–6E and 8B).

Among the large brain stem targets of the SNr, the PPN and MidRF are exceptional in that they receive converging collateral input from all projection pools (Figure 6E) and, thus, are brain stem hubs. Whether these projections mediate general functions, such as muscle tone or arousal (Pienaar et al., 2017), and/or specific functions, such as locomotion, remains to be determined. The PPN is a classic component of the mesencephalic locomotor region (MLR), which mediates striatal effects on locomotion (Garcia-Rill, 1986; Roseberry et al., 2016; Takakusaki et al., 2003). Our data clarify the connections between the SNr and MLR; the SNr broadly targets the PPN component and only weakly innervates the high-speed locomotion component, the cuneiform nucleus (Caggiano et al., 2018; Takakusaki et al., 2003; Figure 2). However, two major nigral targets, the MSC and IC, project extensively to the cuneiform nucleus (CnF) (Figures S4 and 6E; Comoli et al., 2012; Ferreira-Pinto et al., 2018; Mitchell et al., 1988). Thus, the SNr has diverse paths to the MLR; i.e., indirect to the CnF and direct to the PPN and neighboring MidRF. Various output paths from the SNr might support locomotor control under different behavioral contexts and warrant further study.

Basal ganglia outputs via the SNr are distinguished from those emitted by the internal segment of the globus pallidus (GPi) in their extensive brain stem targets (Figure 2). However, the SNr and GPi share common features in that PV-expressing GABAergic GPi neurons also target motor and intralaminar thalamic nuclei as well as the PPN through collateral projections (Parent and De Bellefeuille, 1982; van der Kooy and Carter, 1981). GPi neurons additionally project to the lateral habenula and thus broadcast in a manner similar to SNr outputs. The second major class of output neurons in the GPi, somatostatin-expressing glutamatergic neurons (Shabel et al., 2012; Vincent and Brown, 1986; Wallace et al., 2017), receive striosome input and have putative limbic functions, similar to nigra dopaminergic neurons (Parent and De Bellefeuille, 1982; Rajakumar et al., 1993). Basal ganglia have a broad capacity to directly influence behavioral circuits at diverse levels. The precise roles of each of these projections, outside of the oculomotor system, and their contribution to specific symptoms of basal ganglia pathology remain to be delineated. Although the SNr has been shown to be capable of modulating general behavior functions, such as motor vigor (Turner and Desmurget, 2010), the modularity and intrinsic specialization of its outputs impose specificity and reveal a circuit architecture that can separately control different behaviors.

STAR★METHODS

Detailed methods are provided in the online version of this paper and include the following:

- KEY RESOURCES TABLE
- RESOURCE AVAILABILITY
  - Lead contact
  - Materials availability
  - Data and code availability
- EXPERIMENTAL MODEL AND SUBJECT DETAILS
- METHOD DETAILS
  - Surgical procedures
  - Histology and staining
  - Imaging and anatomical analyses
  - Electrophysiological recordings
- QUANTIFICATION AND STATISTICAL ANALYSIS

SUPPLEMENTAL INFORMATION

Supplemental information can be found online at https://doi.org/10.1016/j.neuron.2021.03.017.

ACKNOWLEDGMENTS

This work was supported by the European Research Council (to R.M.C.); a Howard Hughes Medical Institute grant (to R.M.C.); National Institute of Neurological Disorders and Stroke grants T32 NS007220 (to L.E.M.), U19 NS107466 (to D.K.), U01 NS090595 (to D.K.), R01 NS111162 (to B.L.B.), and U19 NS104649 (to R.M.C.); National Institute of Mental Health grant U01 MH114829 (to B.K.L.); a Tourette Association of America grant (to L.E.M.); and equipment funds from the Dr. George Feher Experimental Biophysics Chair. We thank Agnieszka Brzozowska-Prechtl and Karishma Chhabria for assistance with histology, Beth Friedman for preparing the *in situ* samples, Fan Wang (MIT) for providing the retrograde lentivirus, Hannah Leichty and Alexander Newberry for technical support, Jack Glaser of MicroBrightField Bioscience for use of their Neurolucida software and access to "beta" versions of new programs, and Harvey J. Karten for helpful discussions. D.K. attended to the myriad of university rules and forms that govern environmental health and safety, including ethical use of animals as well as use of chemicals, controlled substances, cybersecurity, hazardous substances, and viruses.

AUTHOR CONTRIBUTIONS

R.M.C., D.K., B.K.L., and L.E.M. conceived the study and designed the experiments. L.E.M. conducted anatomical and electrophysiological experiments. G.S.B. performed *in situ* hybridization experiments. Y.C., D.K., L.E.M., and J.D.M. formulated analysis tools. L.E.M. analyzed data. B.L.B., R.M.C., and D.K. supplied reagents. R.M.C., D.K., and L.E.M. wrote the manuscript.

DECLARATION OF INTERESTS

The authors declare no competing interests.

Received: January 29, 2021
Revised: March 7, 2021
Accepted: March 10, 2021
Published: April 5, 2021

REFERENCES

Aldes, L.D. (1988). Thalamic connectivity of rat somatic motor cortex. Brain Res. Bull. *20*, 333–348.

Alexander, G.E., Crutcher, M.D., and DeLong, M.R. (1990). Basal ganglia-thalamocortical circuits: parallel substrates for motor, oculomotor, "prefrontal" and "limbic" functions. Prog. Brain Res. *85*, 119–146.

Alloway, K.D., Smith, J.B., and Beauchemin, K.J. (2010). Quantitative analysis of the bilateral brainstem projections from the whisker and forepaw regions in rat primary motor cortex. J. Comp. Neurol. *518*, 4546–4566.

Anderson, M., and Yoshida, M. (1977). Electrophysiological evidence for branching nigral projections to the thalamus and the superior colliculus. Brain Res. *137*, 361–364.

Arber, S. (2012). Motor circuits in action: specification, connectivity, and function. Neuron *74*, 975–989.

Arber, S., and Costa, R.M. (2018). Connecting neuronal circuits for movement. Science *360*, 1403–1404.

Asanuma, C., Thach, W.T., and Jones, E.G. (1983). Brainstem and spinal projections of the deep cerebellar nuclei in the monkey, with observations on the brainstem projections of the dorsal column nuclei. Brain Res. *286*, 299–322.

Åström, K.J., and Murray, R.M. (2008). Feedback systems: an introduction for scientists and engineers (Princeton University Press).

Atherton, J.F., and Bevan, M.D. (2005). Ionic mechanisms underlying autonomous action potential generation in the somata and dendrites of GABAergic substantia nigra pars reticulata neurons in vitro. J. Neurosci. *25*, 8272–8281.

Bankhead, P., Loughrey, M.B., Fernández, J.A., Dombrowski, Y., McArt, D.G., Dunne, P.D., McQuaid, S., Gray, R.T., Murray, L.J., Coleman, H.G., et al. (2017). QuPath: Open source software for digital pathology image analysis. Sci. Rep. *7*, 16878.

Beckstead, R.M., and Frankfurter, A. (1982). The distribution and some morphological features of substantia nigra neurons that project to the thalamus, superior colliculus and pedunculopontine nucleus in the monkey. Neuroscience *7*, 2377–2388.

Bentivoglio, M., and Kuypers, H.G. (1982). Divergent axon collaterals from rat cerebellar nuclei to diencephalon, mesencephalon, medulla oblongata and cervical cord. A fluorescent double retrograde labeling study. Exp. Brain Res. *46*, 339–356.

Berendse, H.W., and Groenewegen, H.J. (1990). Organization of the thalamostriatal projections in the rat, with special emphasis on the ventral striatum. J. Comp. Neurol. *299*, 187–228.

Brownstone, R.M., and Chopek, J.W. (2018). Reticulospinal Systems for Tuning Motor Commands. Front. Neural Circuits *12*, 30.

Büttner-Ennever, J.A. (2006). The extraocular motor nuclei: organization and functional neuroanatomy. Prog. Brain Res. *151*, 95–125.

Caggiano, V., Leiras, R., Goñi-Erro, H., Masini, D., Bellardita, C., Bouvier, J., Caldeira, V., Fisone, G., and Kiehn, O. (2018). Midbrain circuits that set locomotor speed and gait selection. Nature *553*, 455–460.

Cebrián, C., and Prensa, L. (2010). Basal ganglia and thalamic input from neurons located within the ventral tier cell cluster region of the substantia nigra pars compacta in the rat. J. Comp. Neurol. *518*, 1283–1300.

Cebrián, C., Parent, A., and Prensa, L. (2005). Patterns of axonal branching of neurons of the substantia nigra pars reticulata and pars lateralis in the rat. J. Comp. Neurol. *492*, 349–369.

Chen, Y., McElvain, L.E., Tolpygo, A.S., Ferrante, D., Friedman, B., Mitra, P.P., Karten, H.J., Freund, Y., and Kleinfeld, D. (2019). An active texture-based digital atlas enables automated mapping of structures and markers across brains. Nat. Methods *16*, 341–350.

Chronister, R.B., Walding, J.S., Aldes, L.D., and Marco, L.A. (1988). Interconnections between substantia nigra reticulata and medullary reticular formation. Brain Res. Bull. *21*, 313–317.

Cicirata, F., Angaut, P., Cioni, M., Serapide, M.F., and Papale, A. (1986). Functional organization of thalamic projections to the motor cortex. An anatomical and electrophysiological study in the rat. Neuroscience *19*, 81–99.

Comoli, E., Das Neves Favaro, P., Vautrelle, N., Leriche, M., Overton, P.G., and Redgrave, P. (2012). Segregated anatomical input to sub-regions of the rodent superior colliculus associated with approach and defense. Front. Neuroanat. *6*, 9.

Dean, P., Redgrave, P., and Mitchell, I.J. (1988). Organisation of efferent projections from superior colliculus to brainstem in rat: evidence for functional output channels. Prog. Brain Res. *75*, 27–36.

DeLong, M.R., and Georgopoulos, A.P. (2011). Motor Functions of the Basal Ganglia. In Comprehensive Physiology, R. Terjung, ed.. https://doi.org/10.1002/cphy.cp010221.

DeLong, M.R., Crutcher, M.D., and Georgopoulos, A.P. (1983). Relations between movement and single cell discharge in the substantia nigra of the behaving monkey. J. Neurosci. *3*, 1599–1606.

Deniau, J.M., Hammond-Le Guyader, C., Feger, J., and McKenzie, J.S. (1977). Bilateral projection of nigro-collicular neurons: An electrophysiological analysis in the rat. Neurosci. Lett. *5*, 45–50.

Deniau, J.M., Menetrey, A., and Charpier, S. (1996). The lamellar organization of the rat substantia nigra pars reticulata: segregated patterns of striatal afferents and relationship to the topography of corticostriatal projections. Neuroscience *73*, 761–781.

Dräger, U.C., and Hubel, D.H. (1976). Topography of visual and somatosensory projections to mouse superior colliculus. J. Neurophysiol. *39*, 91–101.

Economo, M.N., Viswanathan, S., Tasic, B., Bas, E., Winnubst, J., Menon, V., Graybuck, L.T., Nguyen, T.N., Smith, K.A., Yao, Z., et al. (2018). Distinct descending motor cortex pathways and their roles in movement. Nature *563*, 79–84.

Ferreira-Pinto, M.J., Ruder, L., Capelli, P., and Arber, S. (2018). Connecting Circuits for Supraspinal Control of Locomotion. Neuron *100*, 361–374.

Franklin, K.B.J., and Paxinos, G. (2013). Paxinos and Franklin's The mouse brain in stereotaxic coordinates*Fourth edition* (Academic Press).

Fukushima, K. (1987). The interstitial nucleus of Cajal and its role in the control of movements of head and eyes. Prog. Neurobiol. *29*, 107–192.

Gabbott, P.L., Warner, T.A., Jays, P.R., Salway, P., and Busby, S.J. (2005). Prefrontal cortex in the rat: projections to subcortical autonomic, motor, and limbic centers. J. Comp. Neurol. *492*, 145–177.

Garcia-Rill, E. (1986). The basal ganglia and the locomotor regions. Brain Res. *396*, 47–63.

Gerfen, C.R., Herkenham, M., and Thibault, J. (1987). The neostriatal mosaic: II. Patch- and matrix-directed mesostriatal dopaminergic and non-dopaminergic systems. J. Neurosci. *7*, 3915–3934.

Gervasoni, D., Peyron, C., Rampon, C., Barbagli, B., Chouvet, G., Urbain, N., Fort, P., and Luppi, P.H. (2000). Role and origin of the GABAergic innervation of dorsal raphe serotonergic neurons. J. Neurosci. *20*, 4217–4225.

González-Hernández, T., and Rodríguez, M. (2000). Compartmental organization and chemical profile of dopaminergic and GABAergic neurons in the substantia nigra of the rat. J. Comp. Neurol. *421*, 107–135.

González-Hernández, T., Barroso-Chinea, P., Acevedo, A., Salido, E., and Rodríguez, M. (2001). Colocalization of tyrosine hydroxylase and GAD65 mRNA in mesostriatal neurons. Eur. J. Neurosci. *13*, 57–67.

Graybiel, A.M., and Ragsdale, C.W., Jr. (1979). Fiber connections of the basal ganglia. Prog. Brain Res. *51*, 237–283.

Grillner, S. (2006). Biological pattern generation: the cellular and computational logic of networks in motion. Neuron *52*, 751–766.

Gulley, J.M., Kuwajima, M., Mayhill, E., and Rebec, G.V. (1999). Behavior-related changes in the activity of substantia nigra pars reticulata neurons in freely moving rats. Brain Res. *845*, 68–76.

Gulley, J.M., Kosobud, A.E., and Rebec, G.V. (2002). Behavior-related modulation of substantia nigra pars reticulata neurons in rats performing a conditioned reinforcement task. Neuroscience *111*, 337–349.

Haber, S.N., and Calzavara, R. (2009). The cortico-basal ganglia integrative network: the role of the thalamus. Brain Res. Bull. *78*, 69–74.

Hikosaka, O. (2007a). Basal ganglia mechanisms of reward-oriented eye movement. Ann. N Y Acad. Sci. *1104*, 229–249.

Hikosaka, O. (2007b). GABAergic output of the basal ganglia. Prog. Brain Res. *160*, 209–226.

Hikosaka, O., and Wurtz, R.H. (1983). Visual and oculomotor functions of monkey substantia nigra pars reticulata. I. Relation of visual and auditory responses to saccades. J. Neurophysiol. *49*, 1230–1253.

Hikosaka, O., Kim, H.F., Yasuda, M., and Yamamoto, S. (2014). Basal ganglia circuits for reward value-guided behavior. Annu. Rev. Neurosci. *37*, 289–306.

Hintiryan, H., Foster, N.N., Bowman, I., Bay, M., Song, M.Y., Gou, L., Yamashita, S., Bienkowski, M.S., Zingg, B., Zhu, M., et al. (2016). The mouse cortico-striatal projectome. Nat. Neurosci. *19*, 1100–1114.

Hippenmeyer, S., Vrieseling, E., Sigrist, M., Portmann, T., Laengle, C., Ladle, D.R., and Arber, S. (2005). A developmental switch in the response of DRG neurons to ETS transcription factor signaling. PLoS Biol. *3*, e159.

Holmes, A.L., Forcelli, P.A., DesJardin, J.T., Decker, A.L., Teferra, M., West, E.A., Malkova, L., and Gale, K. (2012). Superior colliculus mediates cervical dystonia evoked by inhibition of the substantia nigra pars reticulata. J. Neurosci. *32*, 13326–13332.

Holstege, G. (1987). Some anatomical observations on the projections from the hypothalamus to brainstem and spinal cord: an HRP and autoradiographic tracing study in the cat. J. Comp. Neurol. *260*, 98–126.

Hopkins, D.A., and Holstege, G. (1978). Amygdaloid projections to the mesencephalon, pons and medulla oblongata in the cat. Exp. Brain Res. *32*, 529–547.

Jaccard, P. (1912). The distribution of the flora in the alpine zone. New Phytol. *11*, 37–50.

Jeong, M., Kim, Y., Kim, J., Ferrante, D.D., Mitra, P.P., Osten, P., and Kim, D. (2016). Comparative three-dimensional connectome map of motor cortical projections in the mouse brain. Sci. Rep. *6*, 20072.

Jin, X., and Costa, R.M. (2010). Start/stop signals emerge in nigrostriatal circuits during sequence learning. Nature *466*, 457–462.

Jin, X., and Costa, R.M. (2015). Shaping action sequences in basal ganglia circuits. Curr. Opin. Neurobiol. *33*, 188–196.

Jürgens, U. (2002). Neural pathways underlying vocal control. Neurosci. Biobehav. Rev. *26*, 235–258.

Kita, T., and Kita, H. (2012). The subthalamic nucleus is one of multiple innervation sites for long-range corticofugal axons: a single-axon tracing study in the rat. J. Neurosci. *32*, 5990–5999.

Klaus, A., Alves da Silva, J., and Costa, R.M. (2019). What, If, and When to Move: Basal Ganglia Circuits and Self-Paced Action Initiation. Annu. Rev. Neurosci. *42*, 459–483.

Kolkman, K.E., McElvain, L.E., and du Lac, S. (2011). Diverse precerebellar neurons share similar intrinsic excitability. J. Neurosci. *31*, 16665–16674.

Kolta, A., Morquette, P., Lavoie, R., Arsenault, I., and Verdier, D. (2010). Modulation of rhythmogenic properties of trigeminal neurons contributing to the masticatory CPG. Prog. Brain Res. *187*, 137–148.

Krout, K.E., Belzer, R.E., and Loewy, A.D. (2002). Brainstem projections to midline and intralaminar thalamic nuclei of the rat. J. Comp. Neurol. *448*, 53–101.

Kuypers, H.G.J.M. (2011). Anatomy of the Descending Pathways. In Comprehensive Physiology, R. Terjung, ed.. https://doi.org/10.1002/cphy.cp010213.

Lee, J., Wang, W., and Sabatini, B.L. (2020). Anatomically segregated basal ganglia pathways allow parallel behavioral modulation. Nat. Neurosci. *23*, 1388–1398.

Liang, H., Paxinos, G., and Watson, C. (2011). Projections from the brain to the spinal cord in the mouse. Brain Struct. Funct. *215*, 159–186.

Mandelbaum, G., Taranda, J., Haynes, T.M., Hochbaum, D.R., Huang, K.W., Hyun, M., Umadevi Venkataraju, K., Straub, C., Wang, W., Robertson, K., et al. (2019). Distinct Cortical-Thalamic-Striatal Circuits through the Parafascicular Nucleus. Neuron *102*, 636–652.e7.

Marín, G., Henny, P., Letelier, J.C., Sentis, E., Karten, H., Mrosko, B., and Mpodozis, J. (2001). A simple method to microinject solid neural tracers into deep structures of the brain. J. Neurosci. Methods *106*, 121–129.

May, P.J., Billig, I., Gamlin, P.D., and Quinet, J. (2019). Central mesencephalic reticular formation control of the near response: lens accommodation circuits. J. Neurophysiol. *121*, 1692–1703.

McElvain, L.E., Bagnall, M.W., Sakatos, A., and du Lac, S. (2010). Bidirectional plasticity gated by hyperpolarization controls the gain of postsynaptic firing responses at central vestibular nerve synapses. Neuron *68*, 763–775.

McElvain, L.E., Friedman, B., Karten, H.J., Svoboda, K., Wang, F., Deschênes, M., and Kleinfeld, D. (2018). Circuits in the rodent brainstem that control whisking in concert with other orofacial motor actions. Neuroscience *368*, 152–170.

Mena-Segovia, J., Bolam, J.P., and Magill, P.J. (2004). Pedunculopontine nucleus and basal ganglia: distant relatives or part of the same family? Trends Neurosci. *27*, 585–588.

Mink, J.W. (2001). Basal ganglia dysfunction in Tourette's syndrome: a new hypothesis. Pediatr. Neurol. *25*, 190–198.

Mitchell, I.J., Dean, P., and Redgrave, P. (1988). The projection from superior colliculus to cuneiform area in the rat. II. Defence-like responses to stimulation with glutamate in cuneiform nucleus and surrounding structures. Exp. Brain Res. *72*, 626–639.

Nambu, A. (2011). Somatotopic organization of the primate Basal Ganglia. Front. Neuroanat. *5*, 26.

Nelson, A.B., and Kreitzer, A.C. (2014). Reassessing models of basal ganglia function and dysfunction. Annu. Rev. Neurosci. *37*, 117–135.

Parent, A., and De Bellefeuille, L. (1982). Organization of efferent projections from the internal segment of globus pallidus in primate as revealed by fluorescence retrograde labeling method. Brain Res. *245*, 201–213.

Parent, A., and Hazrati, L.N. (1995). Functional anatomy of the basal ganglia. I. The cortico-basal ganglia-thalamo-cortical loop. Brain Res. Brain Res. Rev. *20*, 91–127.

Parent, A., Mackey, A., Smith, Y., and Boucher, R. (1983). The output organization of the substantia nigra in primate as revealed by a retrograde double labeling method. Brain Res. Bull. *10*, 529–537.

Peters, A.J., Liu, H., and Komiyama, T. (2017). Learning in the Rodent Motor Cortex. Annu. Rev. Neurosci. *40*, 77–97.

Pienaar, I.S., Vernon, A., and Winn, P. (2017). The Cellular Diversity of the Pedunculopontine Nucleus: Relevance to Behavior in Health and Aspects of Parkinson's Disease. Neuroscientist *23*, 415–431.

Pollak Dorocic, I., Fürth, D., Xuan, Y., Johansson, Y., Pozzi, L., Silberberg, G., Carlén, M., and Meletis, K. (2014). A whole-brain atlas of inputs to serotonergic neurons of the dorsal and median raphe nuclei. Neuron *83*, 663–678.

Prensa, L., and Parent, A. (2001). The nigrostriatal pathway in the rat: A single-axon study of the relationship between dorsal and ventral tier nigral neurons and the striosome/matrix striatal compartments. J. Neurosci. *21*, 7247–7260.

Rajakumar, N., Elisevich, K., and Flumerfelt, B.A. (1993). Compartmental origin of the striato-entopeduncular projection in the rat. J. Comp. Neurol. *331*, 286–296.

Raymond, J.L., and Medina, J.F. (2018). Computational Principles of Supervised Learning in the Cerebellum. Annu. Rev. Neurosci. *41*, 233–253.

Redgrave, P., Mitchell, I.J., and Dean, P. (1987a). Descending projections from the superior colliculus in rat: a study using orthograde transport of wheatgerm-agglutinin conjugated horseradish peroxidase. Exp. Brain Res. *68*, 147–167.

Redgrave, P., Mitchell, I.J., and Dean, P. (1987b). Further evidence for segregated output channels from superior colliculus in rat: ipsilateral tecto-pontine and tecto-cuneiform projections have different cells of origin. Brain Res. *413*, 170–174.

Risold, P.Y., Thompson, R.H., and Swanson, L.W. (1997). The structural organization of connections between hypothalamus and cerebral cortex. Brain Res. Brain Res. Rev. *24*, 197–254.

Robbins, J.A., Logemann, J.A., and Kirshner, H.S. (1986). Swallowing and speech production in Parkinson's disease. Ann. Neurol. *19*, 283–287.

Roseberry, T.K., Lee, A.M., Lalive, A.L., Wilbrecht, L., Bonci, A., and Kreitzer, A.C. (2016). Cell-Type-Specific Control of Brainstem Locomotor Circuits by Basal Ganglia. Cell *164*, 526–537.

Rossi, M.A., Li, H.E., Lu, D., Kim, I.H., Bartholomew, R.A., Gaidis, E., Barter, J.W., Kim, N., Cai, M.T., Soderling, S.H., and Yin, H.H. (2016). A GABAergic nigrotectal pathway for coordination of drinking behavior. Nat. Neurosci. *19*, 742–748.

Scheibel, A.B. (2011). The Brain Stem Reticular Core and Sensory Function. In Comprehensive Physiology, R. Terjung, ed.. https://doi.org/10.1002/cphy.cp010306.

Schneider, J.S., Manetto, C., and Lidsky, T.I. (1985). Substantia nigra projection to medullary reticular formation: relevance to oculomotor and related motor functions in the cat. Neurosci. Lett. *62*, 1–6.

Sesack, S.R., Deutch, A.Y., Roth, R.H., and Bunney, B.S. (1989). Topographical organization of the efferent projections of the medial prefrontal cortex in the rat: an anterograde tract-tracing study with Phaseolus vulgaris leucoagglutinin. J. Comp. Neurol. *290*, 213–242.

Shabel, S.J., Proulx, C.D., Trias, A., Murphy, R.T., and Malinow, R. (2012). Input to the lateral habenula from the basal ganglia is excitatory, aversive, and suppressed by serotonin. Neuron *74*, 475–481.

Smith, Y., Raju, D.V., Pare, J.F., and Sidibe, M. (2004). The thalamostriatal system: a highly specific network of the basal ganglia circuitry. Trends Neurosci. *27*, 520–527.

Stanek, E., 4th, Cheng, S., Takatoh, J., Han, B.X., and Wang, F. (2014). Monosynaptic premotor circuit tracing reveals neural substrates for oro-motor coordination. eLife *3*, e02511.

Svoboda, K., and Li, N. (2018). Neural mechanisms of movement planning: motor cortex and beyond. Curr. Opin. Neurobiol. *49*, 33–41.

Takakusaki, K., Habaguchi, T., Ohtinata-Sugimoto, J., Saitoh, K., and Sakamoto, T. (2003). Basal ganglia efferents to the brainstem centers controlling postural muscle tone and locomotion: a new concept for understanding motor disorders in basal ganglia dysfunction. Neuroscience *119*, 293–308.

Towe, A.L., and Luschei, E.S. (2013). Motor Coordination (Springer).

Turner, R.S., and Desmurget, M. (2010). Basal ganglia contributions to motor control: a vigorous tutor. Curr. Opin. Neurobiol. *20*, 704–716.

Utter, A.A., and Basso, M.A. (2008). The basal ganglia: an overview of circuits and function. Neurosci. Biobehav. Rev. *32*, 333–342.

van der Kooy, D., and Carter, D.A. (1981). The organization of the efferent projections and striatal afferents of the entopeduncular nucleus and adjacent areas in the rat. Brain Res. *211*, 15–36.

Vincent, S.R., and Brown, J.C. (1986). Somatostatin immunoreactivity in the entopeduncular projection to the lateral habenula in the rat. Neurosci. Lett. *68*, 160–164.

Visser, J.E., and Bloem, B.R. (2005). Role of the basal ganglia in balance control. Neural Plast. *12*, 161–174, discussion 263–272.

Von Krosigk, M., and Smith, A.D. (1991). Descending Projections from the Substantia Nigra and Retrorubral Field to the Medullary and Pontomedullary Reticular Formation. Eur. J. Neurosci. *3*, 260–273.

Wallace, M.L., Saunders, A., Huang, K.W., Philson, A.C., Goldman, M., Macosko, E.Z., McCarroll, S.A., and Sabatini, B.L. (2017). Genetically Distinct Parallel Pathways in the Entopeduncular Nucleus for Limbic and Sensorimotor Output of the Basal Ganglia. Neuron *94*, 138–152.e5.

Wang, S., and Redgrave, P. (1997). Microinjections of muscimol into lateral superior colliculus disrupt orienting and oral movements in the formalin model of pain. Neuroscience *81*, 967–988.

Yasui, Y., Nakano, K., Nakagawa, Y., Kayahara, T., Shiroyama, T., and Mizuno, N. (1992). Non-dopaminergic neurons in the substantia nigra project to the reticular formation around the trigeminal motor nucleus in the rat. Brain Res. *585*, 361–366.

Yasui, Y., Tsumori, T., Ando, A., Domoto, T., Kayahara, T., and Nakano, K. (1994). Descending projections from the superior colliculus to the reticular formation around the motor trigeminal nucleus and the parvicellular reticular formation of the medulla oblongata in the rat. Brain Res. *656*, 420–426.

STAR★METHODS

KEY RESOURCES TABLE

REAGENT or RESOURCE	SOURCE	IDENTIFIER
Antibodies		
Anti-GFP	Novus Biologicals	Cat#NB600-308; RRID:AB_10003058
Bacterial and virus strains		
AAV-DJ hSyn-FLEX-mGFP-2A-Synaptophysin-mRuby	Stanford Virus Core	Cat#GVVC-AAV-100
R(G)-lentivirus-hSyn-Cre	Wang Lab, MIT	Addgene plasmid #86641
AAV2/2-EF1α-DIO-EYFP	UNC Vector Core	N/A
R(G)-EIAV-DIO-FLP	Lim Lab, UCSD	N/A
AAV-DJ-EF1α-fDIO-EYFP	UNC Vector Core	N/A
Chemicals, peptides, and recombinant proteins		
NeuroTrace 435/455 Blue Fluorescent Nissl Stain	ThermoFisher	Cat#N21479
Alexa 594-conjugated dextran	ThermoFisher	Cat#D22913
Kynurenic acid sodium salt	Abcam	Cat#ab120256
Picrotoxin	Abcam	Cat#ab120315
OPAL 520	Akoya Biosciences	Cat#FP1487001KT
OPAL 620	Akoya Biosciences	Cat#FP1495001KT
OPAL 690	Akoya Biosciences	Cat#FP1497001KT
Critical commercial assays		
RNAscope® Multiplex Fluorescent Reagent Kit v2	ACD	Cat#323100
Vectastain® Elite ABC-HRP Kit	Vector	Cat#PK-6100; RRID:AB_2336819
RNAscope® Probe -Mm-Pvalb	ACD	Cat#421931
RNAscope® Probe -Mm-Slc32a1-C2	ACD	Cat#319191-C2
RNAscope® Probe -Mm-Th-C3	ACD	Cat#317621-C3
RNAscope® Probe -Mm-Gad2-C3	ACD	Cat#439371-C3
Experimental models: Organisms/strains		
B6.129P2-*Pvalb*$^{tm1(cre)Arbr}$/J	The Jackson Laboratory	Stock No. 017320; RRID:IMSR_JAX:017320
C57BL/6J	The Jackson Laboratory	Stock No: 000664; RRID:IMSR_JAX:000664
B6J.129S6(FVB)-*Slc32a1*$^{tm2(cre)Lowl}$/MwarJ	The Jackson Laboratory	Stock No: 028862; RRID:IMSR_JAX:028862
Software and algorithms		
ImageJ	NIH	https://imagej.nih.gov; RRID:SCR_003070
MATLAB	MathWorks	https://www.mathworks.com/products/matlab.html; RRID:SCR_001622
Python, algorithms	Chen et al., 2019	https://github.com/mistycheney/MouseBrainAtlas
VTK Visualization Toolkit		https://vtk.org/; RRID:SCR_015013
Neurolucida	MBF Bioscience	https://www.mbfbioscience.com/neurolucida; RRID:SCR_001775

(*Continued on next page*)

Continued

REAGENT or RESOURCE	SOURCE	IDENTIFIER
Igor Pro 6	Wavemetrics	https://www.wavemetrics.com/order/order_igordownloads6.htm; RRID:SCR_000325
ZEN Digital Imaging Blue 2.0	Carl *Zeiss* Microscopy GmbH	https://www.zeiss.com/microscopy/us/products/microscope-software/zen.html; RRID:SCR_013672
QuPath v0.2.1	Bankhead et al., 2017	https://qupath.github.io; RRID:SCR_018257
Other		
Axio Scan Z.1 Slide scanner microscope	Carl Zeiss Microscopy GmbH	N/A
ORCA-4.0 V3 digital CMOS camera	Hamamatsu	Cat# C13440-20CU
Sliding Microtome	Microm International	Cat #HM400
Nanoject II Auto-Nanoliter Injector	Drummond Scientific	Cat#3-000-204
Microinjector	Creative Instruments Development Company	N/A
Multiclamp 700B Microelectrode Amplifier	Molecular Devices	RRID:SCR_018455
ITC-18	HEKA	N/A
P-97 Flaming/Brown Micropipette Puller	Sutter	RRID:SCR_018636
DMZ Universal Electrode Puller	Zeitz-Instruments	RRID:SCR_014774
Vibratome VT1200S	Leica Biosystems	RRID:SCR_018453

RESOURCE AVAILABILITY

Lead contact

Further information and requests for resources and reagents should be directed to and will be fulfilled by Dr. David Kleinfeld (dk@physics.ucsd.edu).

Materials availability

This study did not generate new unique reagents.

Data and code availability

The datasets and all code supporting the current study are available from the corresponding author on request.

EXPERIMENTAL MODEL AND SUBJECT DETAILS

All experiments were carried out on mice in accordance with the standards of the Guide for the Care and Use of Laboratory Animals and have been approved by Institutional Animal Care and Use Committee at University of California, San Diego and in accordance with the Champalimaud Center for the Unknown Ethics committee guidelines and approved by the Portuguese Veterinary General Board (Direccao Geral de Veterinaria, Ref. No. 0421/000/000/2014). For electrophysiological studies, 72 C57BL/6J mice aged 4-6 weeks were used; for *in situ* labeling, 4 C57BL/6J mice aged 8 weeks were used; and for anatomical mappings, 28 6–8-week-old Parvalbumin-Cre (The Jackson Laboratory, Stock # 01730) (Hippenmeyer et al., 2005), VGAT-Cre (The Jackson Laboratory, Stock #028862), or C57BL/6J mice were used. Animals of both sexes were used in each group of experiments.

METHOD DETAILS

Surgical procedures

All surgeries were performed under sterile conditions. For viral tracing experiments, mice were deeply anesthetized with isoflurane and then placed on either a Kopf stereotax or a custom stereotaxic apparatus with a micromanipulator (Sutter MP-285). Mouse body temperature was maintained at 34°C using an animal temperature controller (ATC1000, World Precision Instruments), and isofluorane was maintained at 1.0%–1.5% (v/v) in oxygen at 1.0 - 1.5 l/min throughout the surgery. For anterograde tracing experiments, craniotomies were made in Parvalbumin-Cre (n = 5) or VGAT-Cre (n = 2) mice using a dental drill over the SNr, and each was unilaterally injected with 40 nL of AAV-DJ hSyn-FLEX-mGFP-2A-Synaptophysin-mRuby (titer = 3×10^{13}, Stanford virus core) with a Nanojet II Injector (Drummond Scientific, USA), which infected approximately 40 - 50% of SNr neurons per experiment. Injections

comprised pulses of 4.6 nl/pulse/minute, and pipets were left in place for 15-20 minutes post-injection. Larger injections were avoided due to spillover into neighboring structures. Animals were sacrificed 5 weeks later. For intersectional SNr collateral mapping experiments, each animal was injected with Rabies-G pseudotyped lentivirus expressing Cre (R(G)-lentivirus-hSyn-Cre, Wang lab, MIT) into a single downstream region and AAV2/2-EF1α-DIO-EYFP-WPRE (UNC virus core) into SNr during the same surgery; animals were sacrificed after 6 weeks (n = 18 mice). For genetic- and projection-specific mapping of collaterals, the same protocol was followed for the injection of R(G)-EIAV-DIO-FLP (Lim lab, UCSD) and AAV-DJ-EF1α-fDIO-EYFP (UNC virus core) (n = 3 mice).

For retrograde tracing for electrophysiolgical recordings, SNr target regions in the thalamus and brainstem were targeted for microinjection of Alexa Fluor-594 dextran (10,000 kD; ThermoFisher) in mice aged 4 - 6 week old mice (average: postnatal day 33 ± 5, n = 56 mice). Injections comprised either a supersaturated solution of dextran in sterile water injected using a Nanojet II Injector (Drummond Scientific, USA) or the placement of solid dextran crystals using a custom-made microinjector (0.2 mm outer diameter, 0.1 mm inner diameter; Creative Instruments Development Company) (Marín et al., 2001). The injection pipette/microinjector was left in place for 15 min post-injection. Mice were sacrificed for electrophysiological experiments 3 - 4 days post-injection. All structures were targeted stereotaxically relative to bregma (See also Figure S5).

Histology and staining

For viral tracing experiments, 5-6 weeks post-injection, animals were deeply anesthetized and transcardially perfused with phosphate-buffered saline (PBS) followed by 4% (w/v) paraformaldehyde (PFA) in PBS. Brains were dissected and post-fixed for 30–60 min in PFA at room temperature, stored overnight at 4°C in PFA, and then transferred to 30% (w/v) sucrose in PBS 12 - 16 hours later. Serial 30-μm coronal sections were cut on a freezing microtome (Microm). Sections were washed with PBS, stained with Neurotrace 435/455 Blue Fluorescent Nissl Stain (1:200, ThermoFisher), wet mounted, and coverslipped with Fluoromount-G (SouthernBiotech). For dark product labeling (Figure S7), sections were counterstained with cytochrome *c* (Sigma) and subsequently stained with anti-GFP primary antibody (Novus) and Vectastain Elite ABC kit (Vector laboratories).

For fluorescence *in situ* hydridizations, mice were deeply anesthetized with Nembutal and decapitated; brains were rapidly dissected, frozen on dry ice in NEG50, and stored at −80C. Serial 20-μm coronal sections were cut on a cryostat, adhered to SuperFrost Plus Slides, and immediately stored at −80C. Sections were fixed in 4% PFA in PBS and stained according to Advanced Cell Diagonstics (ACD) RNAscope Multiplex Fluorescent V2 Assay manual, with the exception of a 1:10 dilution of the Protease IV reagent. Probes for Slc32a1, GAD2, Pvalb, and Th mRNA (ACD) were visualized using Opal dyes (Akoya Biosciences). Slides were counterstained with DAPI. Staining was quantified in SNr and, for control, the dentate gyrus of the same sections using cell segmentation according to size and fluorescent intensity in QuPath (Bankhead et al., 2017).

Imaging and anatomical analyses

Whole-brain slide scanning (20X, NA 0.8) was performed on a Zeiss Axio Scan Z.1 and imaged with a 16-bit Hamamatsu Orca 4.0. Images acquired in Zen software (Zeiss) were exported as 16-bit gray scale tiff files (0.325 μm/pixel). To quantify SNr bouton and axon innervation in downstream brain regions, red and green channel tiffs were read into MATLAB and high-pass filtered and thresholded to subtract autofluorescence. Structure boundary ROIs were defined according to criteria in a standard atlas (Franklin and Paxinos, 2013) using the Neurotrace blue channel in ImageJ. Every 3 - 5 sections were quantified for structures > 300 μm and each section quantified for structures < 300 μm. For axonal collateral quantification, axon density was measured in each structure using a standard 400 μm pixel patch, which restricted the quantification to subnuclear domains in thalamus to respect the topographical organization of collaterals in these nuclei.

Three-dimensional reconstructions of the locations of retrogradely labeled SNr neurons were done in Neurolucida (MBF Bioscience). Fluorescently labeled neurons in SNr were marked manually, and contours of SNr, the whole-brain, and nearby landmarks (red nucleus, oculomotor nucleus, and fasciculus retroflexus) were drawn based on Neurotrace Nissl textures. Three-dimensional stacks were generated based on contour boundaries for each experiment, and individual stacks were aligned in Python to a brainstem model (Chen et al., 2019) by rigid global transformations that maximized the overlap of SNr, the red nucleus, and the oculomotor nucleus. The composite reconstruction of SNr topography was rendered using the Visualization Toolkit (VTK) v.7.1.1 in Python.

The topography of SNr collateral projections in thalamus was analyzed using semi-automated pipeline that interfaced MATLAB and Neurolucida. Zeiss CZI files were analyzed in MATLAB using the Bio-formats/MATLAB package, and putative axon terminal zones were automatically identified using segmentation based on intensity and size criteria. Section outlines were automatically contoured based on intensity of the Neurotrace Nissl, and serial sections were automatically stacked based on an iterative closest point (ICP) algorithm of section outlines. Automated MATLAB reconstructions were converted to a Neurolucida-readable format, and Neurolucida was subsequently used to verify the accuracy of automated contouring and axon identifications. Nucleus boundaries were manually contoured based on Neurotrace Nissl textures. Replicate experiments were aligned to corresponding atlas section (Franklin and Paxinos, 2013) using ICP. Topography was quantified based on 1) the Euclidean distances between centroid locations of each axon terminal field and 2) the weighted Jaccard, denoted $J_{W,}$ based on a 50-μm smoothed axon terminal density within thalamic nuclei, such that for each pair of collateral experiments, A and B:

$$Jw(A,B) = \frac{\sum_k \min(A_{k,}\, B_k)}{\sum_k \max(A_{k,}\, B_k)}$$

where k is the number of samples across space and animals.

Volumes of neuroanatomical regions downstream of SNr were computed using the combination of a publicly available database and manual corrections as needed. Volumes were computed from the Allen Brain Atlas common coordinate framework (CCF v3) for structures whose CCF boundaries adhered to those commonly used (Franklin and Paxinos, 2013). For structures that were not in the CCF or differed significantly, boundaries were manually drawn onto the Allen Brain Atlas images using the Paxinos criteria to calculate their volume in the CCF space. These structures included: ventroanterior thalamus; parvocellular division of the red nucleus; parafascicular region; Pre-Edinger Westphal; the lateral, central, and medial divisions of the superior colliculus; dorso- and ventrolateral periaqueductal gray; precuneiform and cuneiform; rostral interstitial; and prerubral field. Note that no SNr projections were observed in the rostral half of the mediodorsal thalamic nucleus, and measurements of its bouton density and volume were restricted to its caudal half.

Anatomical experiments were excluded from analysis in the following cases: AAV expression spilled into overlaying structures or too few cells were labeled for robust axonal measurements.

Electrophysiological recordings

Mice were deeply anesthetized with Nembutal and decapitated. After rapid dissection in ice cold Ringer's solution (125 mM NaCl, 3.5 mM KCl, 1.0 mM $MgSO_4$, 26 mM $NaHCO_3$, 2.5 mM $CaCl_2$, 1.0 mM NaH_2PO_4, and 11 mM dextrose), 250-300 μm thick coronal slices were cut on a Leica VT1200S vibratome and allowed to recover at 34°C for 30 min. Slices rested at room temperature before being transferred to a recording chamber and being perfused with carbogenated Ringer's containing 125 mM NaCl, 3.5 mM KCl, 1 mM $MgSO_4$, 26 mM $NaHCO_3$, 1.5 mM $CaCl_2$, 1.0 mM NaH_2PO_4, 11 mM dextrose, 100 μM picrotoxin and 2.0 mM kynurenic acid at 34°C.

Patch pipettes were pulled from flame-polished glass (Warner) with resistances of 2-4 MΩ using a pipette puller (Sutter or DMZ). Pipette internal solution contained 140 mM K gluconate, 20 mM HEPES, 8 mM NaCl, 0.1 mM EGTA, 2 mM Mg-ATP, and 0.3 mM Na_2-GTP. Retrogradely labeled neurons were visualized with an epifluorescence 594 filter cube, as well as under infrared differential interference contrast (DIC) illumination with Nomarski optics. Locations of recorded neurons were imaged at 2X under brightfield with condenser aperture reduction for enhanced contrast. Neurons were verified to be in SNr using proximal anatomical landmarks, including the shape and location of the cerebral peduncle, oculomotor nerve, zona incerta, geniculate nuclei, medial and lateral lemnisci, and pontine nuclei. Data were acquired with a Multiclamp 700B, low-pass filtered at 10 kHz and digitized at 40 kHz (ITC-18, HEKA). House-written code in Igor Pro 6 was used for acquisition and analysis. Recordings were corrected for a 14 mV junction potential. Spontaneous firing was measured immediately after break in; maximum firing, gain, and rebound measurements made on top of a 10-Hz baseline firing rate. Maximum firing rate was defined as the maximum mean firing rate sustained during a 1 s-long depolarizing step. Recordings were excluded from analyses if spike height was < 50 mV or series resistance exceeded 15 MΩ.

QUANTIFICATION AND STATISTICAL ANALYSIS

Statistical significance was evaluated for the electrophysiological properties of identified projection populations (Figure 5E) versus those of randomly targeted SNr neurons using the Kruskal-Wallis nonparametic multiple group comparison followed by the Dunn post hoc test performed in GraphPad Prism (version 7.0). To evaluate differences in the composite electrophysiological properties of each pair of projection populations (Figure 5F), the property values were z-scored, and the Euclidean distance between each pair of neurons in normalized parameter space was calculated for all neuron pairs across the two populations. Statistical significance was assessed by data resampling: specifically, the calculated mean pairwise Euclidean distance was compared to a null distribution generated by randomly shuffling the identities of the neurons in the two populations in MATLAB.

To quantify differences in the topography of axon collateral fields in thalamic nuclei (Figure 7E), the mean Euclidean distance between the centroids of the collateral field puncta distributions was computed. Statistical significance was assessed by data resampling in MATLAB. Specifically, we first computed the Euclidean distance across experiments from two different target populations and for experimental replicates of the same target populations. We next randomly resampled each puncta distribution with replacement to generate a bootstrapped distribution of distances and identified pairs of target populations for which the centroid distance across the pair was significantly greater. The weighted Jaccard index was used to quantify the overlap extent of collateral fields in thalamus (Figure S8). To assess its significance, first the index was calculated pairwise across replicates and compared to the null distribution of pairwise Jaccard index generated by shuffling the identity of all experiments.

Data are represented as mean ± SEM unless otherwise indicated. The n numbers and p values are reported explicitly in the main text, figures, and figure legends.